In-situ dissolution rates of silicate minerals and associated bacterial communities in the critical zone (Strengbach catchment, France)

Bastien Wild, Damien Daval, Emilie Beaulieu, Marie-Claire Pierret, Daniel Viville, Gwenaël Imfeld

In-situ Dissolution Rates of Silicate Minerals and Associated Bacterial Communities in the Critical Zone (Strengbach catchment, France)

Bastien Wild[1,2], Damien Daval[1], Emilie Beaulieu[1], Marie-Claire Pierret[1], Daniel Viville[1], Gwenaël Imfeld[1]

[1]*Laboratoire d'Hydrologie et de Géochimie de Strasbourg (LHyGeS), Université de Strasbourg /EOST-CNRS UMR 7517, 1 Rue Blessig, 67000 Strasbourg, France*

[2]*Andlinger Center for Energy and the Environment, Princeton University, Princeton, NJ 08544, USA*

Corresponding author: bwild@princeton.edu

Manuscript submitted to Geochimica et Cosmochimica Acta

ABSTRACT

Weathering of silicate minerals in the Critical Zone (CZ) is fundamental for numerous environmental and societal issues. Despite decades of efforts to accurately record biogeochemical variables controlling mineral reactivity in the field and to reproduce them in the laboratory, weathering rates estimates still differ from those observed in natural settings. Here we examine the biogeochemical environment of mineral surfaces exposed to contrasted weathering conditions in various compartments of a temperate CZ (Strengbach observatory, France). A novel approach was developed to probe both *in-situ* mineral dissolution rates and bacterial diversity associated to mineral surfaces. Labradorite and olivine minerals were either buried in the A and C horizons of a soil profile, directly exposed to meteoric fluids or immersed in stream water. Dissolution rates recorded in the soil profile were up to 2 orders of magnitude slower than those predicted using a numerical weathering model. Samples directly exposed to meteoric fluids exhibited contrasted dissolution rates that could not be explained by simple abiotic weathering, while dissolution rates of samples incubated in stream water were particularly low. In soil profiles, the field-laboratory discrepancy by up to 2 orders of magnitude was attributed to heterogeneity of fluid circulation and local variation of reaction conditions. Mineral substrates changed bacterial communities of the mineralosphere after 9 and 20 months of incubation in the CZ. However, we observed that this effect could be delayed or driven by extrinsic factors. Although mineral probes in soil horizons were enriched in bacterial phylotypes potentially involved in mineral weathering (e.g., *Pseudomonas* sp., *Collimonas* sp., *Burkholderia* sp., *Janthinobacterium* sp., *Leifsonia* sp., and *Arthrobacter* sp.), the relative contribution of biotic weathering could not be quantified *in-situ*. Altogether, the heterogeneity of *in-situ* mineral dissolution rates in key compartments of the CZ reveals the crucial need to improve spatial characterization of hydrogeochemical properties at the soil profile scale, and to evaluate the quantitative role of microbial communities to mineral weathering.

1. INTRODUCTION

Weathering of primary minerals and associated fluxes involved in elemental cycling in natural settings are relevant for numerous environmental and societal challenges. Important issues include the management of inorganic nutrients stocks in soils with the development of sustainable agricultural and forestry practices (Johnson et al., 2015; Klaminder et al., 2011; Lucas et al., 2011; van der Heijden et al., 2013), the contamination of ecosystems due to mining activities (Yu et al., 2014), or long-term forecast of atmospheric CO_2 concentrations (Beaulieu et al., 2012).

Studies on (bio)weathering rates at global (Gaillardet *et al.*, 1999), regional (Gaillardet *et al.*, 1995; Negrel *et al.*, 1993), local (Augusto *et al.*, 2000; Feger *et al.*, 1990; Klaminder *et al.*, 2011) or micro scales (Bonneville *et al.*, 2016; Fischer *et al.*, 2012; Li *et al.*, 2016) underscore that the knowledge of mineral dissolution rates in the critical zone (CZ) remains incomplete. Field weathering rates are usually determined with indirect methods, such as measurements of U-series nuclides in soils and weathering profiles (Ackerer et al., 2016), the monitoring of changes in solid-state regolith compositions (White et al., 1996) and/or geochemical mass-balances over large space and time scales (Velbel, 1993). These rates are often inconsistent with those measured in the laboratory (White and Brantley, 2003). This "field-lab discrepancy" (Paces, 1983; White and Brantley, 2003; Zhu *et al.*, 2014) has stimulated intensive research to reduce uncertainties on element budgets in natural settings. For instance, several types of indirect field measurement approaches were combined to yield estimates of *in-situ* mineral weathering rates (Ackerer *et al.*, 2016; Ferrier *et al.*, 2010). In parallel, mineral dissolution kinetics were evaluated in the laboratory by monitoring dissolution rates against controlled parameters, such as T, pH or ΔG_r (Carroll and Knauss, 2005; Gruber et al., 2014; Hellmann and Tisserand, 2006). This framework allowed to build up databases of parameters used in semi-empirical mineral weathering rate laws (Palandri and Kharaka, 2004; Rimstidt *et al.*,

2012). While this overall strategy has the merit to combine data from independent "top-down" (field measurements) and "bottom-up" (lab experiments) approaches, a consistent theory for mineral weathering in the field is still missing. One possible reason is that "top-down" and "bottom-up" approaches consider different processes, which are recorded on distinct temporal and spatial scales.

Most field studies integrate mineral weathering over large space scales, which do not capture the details of the biogeochemical processes at stake. Field studies may thus fail to provide a mechanistic understanding of *in-situ* mineral weathering, although relevant data for past and current weathering in the critical zone have been produced. Estimates of field weathering rates remain, however, several orders of magnitude greater than laboratory estimates that feed common rate laws used in reactive transport models (Maher et al., 2004; White and Brantley, 2003).

In addition, inconsistent timescales considered in the laboratory and in the field may result in contrasted mineral dissolution rates due to intrinsic factors, i.e. related to the intrinsic crystal chemistry of the weathered phase, or extrinsic factors, i.e. related to the reacting environment of the crystal (Beig and Luttge, 2006; Gruber et al., 2014; White and Brantley, 2003). Indeed, the physicochemical properties of the fluid/silicate interface may change over time during mineral dissolution, depending on weathering conditions (Daval et al., 2011; Wild et al., 2016). As a result, the dissolution rate of mineral surfaces aged over geologic time scales in the field cannot be directly compared to that of pristine mineral surfaces used in the laboratory, resulting in inconsistent estimates of mineral weathering rates. Moreover, silicate mineral dissolution is too slow under typical field conditions to be measured directly with sufficient accuracy. As a result, most studies on silicate dissolution kinetics have been restricted to the investigation of abiotic, far-from-equilibrium conditions (extreme pH and/or temperature conditions) in

laboratory setups. These experimental conditions might change the nature of the elementary processes actually driving mineral dissolution compared to those prevailing in the field.

To sum up, (i) mineral dissolution rates measured in the field and in the lab over contrasted time and space scales may not account for the same processes, (ii) local physicochemical environments controlling mineral dissolution rates in the CZ can hardly be probed, and (iii) laboratory conditions, which are generally controlled, homogeneous, constant and abiotic (or which do not involve (multiple) (micro)organisms), might only partly reflect processes ongoing in the field. In that sense, the strict addition of numerous processes observed independently in simple laboratory set-ups (e.g., abiotic, high temperature, short timescales, etc.) may fail to reproduce mineral weathering in natural settings. Nevertheless, parameters derived from laboratory experiments are directly used in reactive transport codes (Gerard *et al.*, 1996; Steefel and Lasaga, 1994; Yeh and Tripathi, 1991) or in chemical weathering models at the catchment scale (Godderis *et al.*, 2006; Sverdrup and Warfvinge, 1995). Current models may thus partly fail to account for extrinsic and intrinsic processes, possibly resulting in a limited agreement between simulation outputs and measurements of field weathering rates.

While several models integrate element recycling by vegetation and soil acidity controlled by heterotrophic and autotrophic respiration (Beaulieu *et al.*, 2012; Godderis *et al.*, 2006; Roelandt *et al.*, 2010), the influence of microorganisms on *in-situ* mineral dissolution is currently missing. However, microorganisms have been recognized to interact with mineral substrates (Bennett *et al.*, 1996; Uroz *et al.*, 2009; Uroz *et al.*, 2015), and to impact mineral weathering directly or indirectly. For instance, microorganisms can control locally the thermodynamic activity of species in solution by biofilm production (Barker and Banfield, 1996) or produce organic molecules (either organic acids, ligands or siderophores), which may result in organic-metal chelation (Drever and Stillings, 1997) or ligand-promoted dissolution (Ganor *et al.*, 2009; Welch and Ullman, 1993). Microorganisms can also impact mineral weathering by modifying

redox (Lower *et al.*, 2001; Newman and Kolter, 2000; Reguera *et al.*, 2005; Roden *et al.*, 2010) or acid-base conditions (Alisa Mast and Drever, 1987), or even by inducing mechanical stress (Bonneville *et al.*, 2009; Li *et al.*, 2016). The effect of individual microbial strains on mineral weathering has been extensively characterized in controlled systems (Brantley *et al.*, 2001; Kalinowski *et al.*, 2000). However, this approach relies on the selection of culturable strains, which accounts for much less than 1% of the microorganisms occuring in many environments (Solden et al., 2016). Some model microorganisms may thus be selected based on cultivation restrictions (van Scholl et al., 2008) rather than for their actual effect or relevance for mineral weathering. To date, most available bioweathering studies have been considering axenic cultures, with the exception of some recent attempts to use field-relevant microbial communities (Wild et al., 2018). In addition, planktonic cells are generally considered, while biofilms, are often neglected in weathering studies. Altogether, this questions the environmental relevance of experiments conducted with model cultures to infer weathering rates under field conditions. Identifying the weathering potential of microbial communities, as well as their contribution to global weathering fluxes, remains a challenging but fundamental issue that remains largely unexplored.

Another important gap between laboratory and field conditions is the consideration of microbial communities in nutrient-poor environments. While microorganisms influence mineral dissolution rates, the mineral substratum may reciprocally influence microbial communities {Bennett, 2001; Certini, 2004; Gleeson, 2005; Gleeson, 2006; Mitchell, 2013; Rogers, 2004; Uroz, 2012; Wild, 2018}. Minerals can thus constitute an ecological niche called the mineralosphere (Uroz et al., 2015). However, factors controlling the interplay between microbial composition and mineral weathering in natural settings remain poorly known.

In this context, the purpose of this study was to evaluate *in-situ* mineral dissolution rates in key compartments of the CZ, to assess the physicochemical parameters controlling the

dissolution process and to evaluate its impact on bacterial communities. We incubated *in-situ* fresh mineral powders and polished surfaces (i.e., prepared in the laboratory) directly in environmental settings. This approach attempts to bridge field and laboratory measurements by probing *in-situ* (or "on site") field weathering rates, and by integrating all biotic and abiotic factors contributing to silicate mineral weathering in the field. Mineral dissolution and bacterial communities associated to different types of silicates (see section 2.1) were directly probed in different compartments of the Strengbach Critical Zone Observatory (CZO, Eastern France). Targeted compartments included (i) rocks in open-air weathering conditions (i.e., direct exposure to meteoric fluids), (ii) two contrasted soil compartments (A and C soil horizons), and (iii) the Strengbach stream at the outlet of the watershed. Direct field estimates of mineral weathering rates were compared to rates predicted with the WITCH model (Godderis *et al.*, 2006) relying on dissolution rate laws derived from laboratory measurements. This enabled to identify factors contributing to the field-laboratory discrepancy. In parallel, bacterial 16S rRNA gene surveys were conducted using high-throughput sequencing to explore the diversity of microbial communities associated to weathered minerals. Amongst all possible actors for microbial weathering, we focus here on bacteria, whose role in mineral weathering have already been extensively described in literature (see, e.g. Uroz *et al.*, 2015 for a review).

2. METHODS

2.1. Mineral selection

Labradorite, olivine and quartz were selected for this study as model minerals. Labradorite is a tectosilicate belonging to the plagioclase feldspar series, which prevails in the continental crust. Labradorite is a rather reactive feldspar with an approximately halfway composition between albite and anorthite end-members. It contains Na, Ca and some K cations, whose pools may be threatened by some forestry practices in temperate forest ecosystems (Johnson *et al.*,

2015; Lucas *et al.*, 2011; van der Heijden *et al.*, 2013). The labradorite used in this study originates from Madagascar and has the following average composition: $Na_{0.5}Ca_{0.5}Al_{1.5}Si_{2.5}O_8$ (Wild *et al.*, 2016). The olivine used here originates from San Carlos and has a composition close to the pure forsterite pole ($Fo_{92.0\pm1.3}$), as determined by inductively coupled plasma atomic emission spectroscopy (ICP-AES) after a standard lithium metaborate fusion. Olivine is a nesosilicate that is characteristic of mafic to ultramafic geological settings. While this mineral is exogenous to the geological context of the study site, it contains Fe and Mg, which are relevant micronutrients in forest ecosystems, and especially for the Strengbach catchment. Fe is a limiting nutrient in most of aerobic natural settings (Johnstone and Nolan, 2015) due to its rapid oxidation kinetics (Davison and Seed, 1983) and its low biodisponibility (Saha *et al.*, 2013). Deficiency in bioavailable Mg has been reported for the Strengbach CZ (Bonneau *et al.*, 1991; Dambrine *et al.*, 1992). Quartz was provided by the Museum of Mineralogy of Strasbourg (France). Quartz is nutrient-free, and it was used in parallel as a non-weatherable reference under the reacting conditions and over the time scales considered (Knauss and Wolery, 1988; Tester *et al.*, 1994).

2.2. Study site

Mineral samples were incubated at the Strengbach catchment (Observatoire Hydrogéochimique de l'Environnement, Alsace, France; 48°12'48.33''N; 7°12'2.23''E, 1146 m (summit) to 883 m (outlet)), involved French and international critical zone observatories networks (OZCAR, http://www.ozcar-ri.org/; RBV, http://portailrbv.sedoo.fr/?locale=en#CMSConsultPlace:HOME; CZEN, http://www.czen.org/content/strengbach-catchment-ohge). The Strengbach stream drains a surface area of 80 ha (Fig. 1 A). Forested land comprises 80 % of conifers (*Picea abies*), and 20% of lobed-leaved trees, dominated by *Fagus sylvatica* spp.

199 The watershed lies on a granitic bedrock, mainly composed of a Hercynian base-poor
200 granite (cordieritic granite) with low Ca and Mg contents, which has been strongly
201 hydrothermally altered on the northern slope and comparatively weakly altered on the southern
202 slope. The top of the northern slope is covered by a 20 to 30 m -thick gneiss layer. Several
203 microgranite intrusions occurred in the southern face (El Gh'Mari, 1995; Pierret *et al.*, 2014).
204 The soils of the watershed range from ochre podzolic soils to brown acidic soils (Lefèvre,
205 1988). Since 1985, the OHGE is fully equipped for continuous monitoring of climatic and
206 hydrogeochemical parameters (Pierret *et al.*, 2014; Viville *et al.*, 2012). Climatic data were
207 obtained from a weather station (Fig. 1 A).
208 The pedological parameters of 10 soil samples collected at the beech plot on 11/18/2013
209 and 12/02/2014 were analyzed at INRA, Arras, France (Tables A.1-A.4; Fig. 1B). About 1 kg
210 of soil samples was collected at several depths along a 120 cm depth soil profile. Water content
211 was estimated by weighing samples before and after drying at 110°C. Soil samples were
212 quartered and sieved (2 mm) as described in previous studies (Duplay *et al.*, 2014; Lucas *et al.*,
213 2011). Granulometry and organic fractions were determined according to SOL-0303 and SOL-
214 0401 standardized procedures, respectively.
215
216 **2.3. Experimental setting**
217 Two sets of mineral probes were incubated simultaneously into four contrasted
218 compartments of the CZ (atmosphere, A and C soil horizons and stream). The mineral probes
219 were collected separately after 9 and 20 months to evaluate temporal changes. Each set of
220 probes consisted of two types of probes: (i) the integrative reactivity probes to estimate *in-situ*
221 dissolution rates of labradorite, olivine and quartz, and (ii) the environmental probes to
222 characterize bacterial communities associated to each mineral.
223

2.3.1. Integrative reactivity probes

The integrative reactivity probes consisted of fresh mineral surfaces of labradorite and olivine prepared by polishing raw materials to eliminate the impact of surface ageing on surface reactivity. A Room Temperature Vulcanizing (RTV) glue mask was deposited on each polished surface to enable direct measurements of the mean mineral weathering rates *in-situ*, integrated over the incubation time, by comparing the topography of the mineral sample before and after incubation (Wild *et al.*, 2016; see also section 2.4). Reactivity of samples is quantified in terms of surface-normalized dissolution rates ($mol.m^{2}.s^{-1}$) throughout this article.

Samples were cleaned with ethanol and packed into 100 µm-calibrated mesh nylon cloth (Fisher Scientific, Pittsburgh, PA) to allow circulation of soil fluids and microorganisms. Each nylon bag was individually sealed by sewing with 0.12 mm nylon thread. Bags were sterilized, and DNA was eliminated under UV light and rinsed with 0.2-µm filtrated ethanol. Bags were then dried under laminar flow and kept sterile until incubation at the Strengbach catchment (see Fig. 1-A, and section 2.3.3).

2.3.2. Environmental probes

The environmental probes consisted of nylon bags filled up with sterile labradorite, olivine and quartz powders for bacterial colonization. Powder preparation and sterilization was performed as described in Wild *et al.* (2016) and Wild *et al.* (2018). Briefly, olivine, labradorite and quartz crystals were crushed with a hydraulic press, and the powder was dry sieved to recover the 160-315 µm fraction (Fig. A.1). Residual fine particles were removed by successive sonication steps in ethanol, and the removal of particles was assessed by SEM observations. The specific surface area of powders was measured using the Brunauer-Emmet-Teller method (BET, Brunauer *et al.*, 1938). Powders were washed for 10 minutes in sterile vessels with two successive baths of 0.2 µm filtered absolute ethanol, dried for >60 min under sterile laminar

flow and exposed to ultraviolet radiation for 20 min. A known amount of powder (2.5-3.5 g) was then sealed in a nylon bag allowing circulation of environmental fluid and microorganisms. Environmental probes were further cleaned and sterilized prior to their incubation at the Strengbach catchment as described previously. Empty control bags were added to each set to evaluate the effect of the nylon bag on bacterial communities.

2.3.3. Incubation of the probes in CZ compartments

A first set of probes was fixed to a perforated Polytetrafluoroethylene (PTFE) plate allowing rainfall to flow across the nylon bags (Fig. 1E and 1F). Probes were placed at the weather station (Fig. 1A; 48°13'0.56"N; 7°11'47.82"E). Samples were directly exposed to atmospheric weathering (wind, rainfall and meteoric deposits). This "meteoric" compartment represents the entry point at the atmosphere-soil interface of the CZ, which is not influenced by soil hydrological or pedogenesis processes.

Two other sets of probes were incubated into the A-horizon (10-cm depth) and the C-horizon (>60 cm) of the soil profile (Fig. 1B) of the reference beech plot (48°12'41.04"N; 7°11'45.66"E). This plot was selected as it combines higher rainfall volumes (northern slope), simple topography (single slope, Fig. 1A) and homogeneous soil and forest covers. Incubation depths corresponded to that of zero-tension lysimetric plates collecting soil solutions since 1992. Mean pH of solutions from A-horizon was 4.22 ± 0.17 (1992-2016 period, n =178 measurements). In the C horizon, a lower dissolution rate is expected due to higher pH values (mean ± SD: 4.89 ± 0.28; 1992-2016 period, n = 104 measurements). Overall, hydrological, geochemical and microbial processes at the A-horizon (topsoil, leaf litter) and the C-horizon (saprolite) are expected to differ.

The fourth set was incubated in the Strengbach stream, at the outlet of the watershed (48°13'0.56"N; 7°12'20.95"E), to allow for a permanent fluid-mineral contact. Samples were

inserted into PTFE tubes and oriented along stream flow (Fig. 1H and 1I). The average pH of the stream measured at the outlet was 6.46 ± 0.24 for the period of incubation (2014/2015).

The sets of probes were collected separately after 9 months (from March 3rd, 2014 to December 2nd, 2014) and 20 months (from March 3rd, 2014 to November 9th, 2015) using sterile forceps. The probes were individually placed into sterile 50 mL Falcon tubes and transported into the laboratory in a sealed cooler and further handled under sterile laminar flow. Probes were collected during the same season (fall) to limit seasonal effects on microbial communities of the mineralosphere (Uroz *et al.*, 2011).

2.4. Measurement of mineral weathering rates

Vertical scanning interferometry (VSI, Zygo New View 7300) was used to estimate mineral weathering rates r, based on the global retreat (Δz) of the surface of each integrative reactivity probe after incubation, compared to an unreacted (masked) portion of the same mineral surface, as follows:

$$r = \frac{\Delta \mathrm{z}}{\Delta t * V_m} \quad (1)$$

where Δt stands for the incubation duration and V_m is the molar volume of the considered mineral. This approach was previously shown to provide dissolution rates consistent with classical powder dissolution experiments (Arvidson et al., 2003; Arvidson and Luttge, 2010; Daval et al., 2013), and has been applied here for the first time in the field.

2.5. Predictions of mineral weathering rates

The WITCH model (Godderis *et al.*, 2006) was used to evaluate mineral dissolution rates of samples incubated in soils. The model used physicochemical parameters recorded *in-situ* during mineral incubation. WITCH enabled to reproduce *in-situ* reactivity conditions (e.g. parameters of the reactive fluids including T, pH and more generally, solution composition) at

298 stake during probe incubation using the OHGE database (1987-2016). Modeled mineral
299 dissolution rates relying on kinetic rate laws derived from previous laboratory weathering
300 experiments were compared to *in-situ* measurements based on integrative reactivity probes
301 (field rates). Input parameters of WITCH model such as the solubility products of secondary
302 phases were previously adjusted in a wide variety of contexts (Beaulieu et al., 2012; Beaulieu
303 et al., 2010; Godderis et al.; Violette et al., 2010). Therefore, differences between modeled and
304 observed dissolution rates were interpreted here in terms of field-lab discrepancy.

305 Briefly, the model considered a one-dimensional soil profile discretized into 36
306 homogeneous boxes of 5-cm height overlying a bedrock layer. At each time step, the code
307 solves the following mass-balance equation for each box:

$$\frac{dC}{dt} = F_{up} - F_{down} + F_{weath} - F_{prec} + F_{ex} + F_{veg} \quad (2)$$

308 where C is the concentration of a given dissolved species in the considered box. F_{up} represents
309 the input flux at the top of the considered box through drainage while F_{down} is the output flow
310 through downward drainage. F_{weath} and F_{prec} stand for the release of a given species from
311 primary minerals through weathering processes or for its consumption by the precipitation of
312 secondary phases, respectively. F_{ex} and F_{veg} stand for the fluxes associated to the exchange of
313 this species with the argilo-humic complex or with the vegetation (either nutrient consumption
314 or organic matter decay), respectively. Input fluxes were estimated by a series of rain gauges
315 and an experimental setup at the beech plot dedicated to throughfall and soil solution collection
316 (Prunier *et al.*, 2015, http://ohge.unistra.fr/). Output elemental fluxes from the watershed were
317 quantified by an experimental hutch located at the catchment outlet, where water discharge,
318 solute concentrations, suspended matter and sediments are continuously quantified (Viville *et*
319 *al.*, 2012). Fluxes related to mineral weathering were calculated as follows:

$$F_{weath} = Area_{Min} * \phi_{Min} * SMS * x_{molar} * R_{min} \quad (3)$$

where $Area_{Min}$ corresponds to the mineral specific surface area in $m^2_{mineral}.m^{-3}_{soil}$, ϕ_{Min} stands for the volumetric proportion of that mineral in the considered soil horizon, x_{molar} is the stoichiometric coefficient of the element of interest in the considered mineral. SMS refers to the soil moisture saturation (Sverdrup, 1990; Sverdrup and Warfvinge, 1993; Warfvinge and Sverdrup, 1992):

$$SMS = \frac{\theta * \rho_{solid}}{\rho_{solid} - \rho_i + \theta * \rho_{water}} \quad (4)$$

where ρ_{solid} and ρ_{water} are the density of the soil particles and water respectively (kg.m^{-3}), ρ_i is the bulk density of the soil and θ is the dimensionless soil water content. The water content of each soil layer and the vertical drainage used by the WITCH model were estimated using the BILJOU© model (Granier *et al.*, 1999).

R_{min} $(mol.m^{-2}.s^{-1})$ is the mineral weathering rate defined as:

$$R_{min} = \left[\sum_i A_{i,min}.exp\left(\frac{-E^i_{a,min}}{RT}\right).a_i^{n_{i,min}}\right](1-\Omega^S) \quad (5)$$

where $A_{i,min}$ $(mol.m^{-2}.s^{-1})$ is the Arrhenius pre-exponential factor, R $(J.mol^{-1}.K^{-1})$ the gas constant and T (K) the absolute temperature, respectively. $E^i_{a,min}$ $(J.mol^{-1})$ is the activation energy, a_i the dimensionless ion activity and $n_{i,min}$the dimensionless reaction order with respect to the hydrolysis of mineral min by the reactive species i (either H^+, OH^-, H_2O or an organic ligand). Ω is the dimensionless mineral saturation index and S is a dimensionless empirical fitting parameter (Maher *et al.*, 2009) assimilated to a "stoichiometric number" (Goddéris and Donnadieu, 2009; Godderis *et al.*, 2006) equal to 1 for olivine and to 1/3 for labradorite according to the WITCH database.

The soil mineral specific surface area was estimated from soil texture according to a parametric law (Sverdrup and Warfvinge, 1995):

$$Area_{Min} = \rho * (8.0 * X_{clay} + 2.2 * X_{silt} + 0.3.* X_{sand}) \quad (6)$$

where ρ is the density of the considered soil layer, and X_{clay}, X_{silt}, and X_{sand} correspond to the clay, silt and sand fraction, respectively, with

$$X_{clay} + X_{silt} + X_{sand} = 1 \quad (7)$$

Soil texture (different fractions), density and porosity were measured on-site for the superficial and the deep layers (5- and 150 cm-depth respectively). The average composition of top and deep soil layers considered to run simulations were: 15% clay, 19% silt and 66% sand, and 9% clays, 19% silt and 72% sand, respectively (according to Table A.2 and Beaulieu *et al.*, 2016). The mineralogical composition in each box was calculated by linear interpolation of the measured data given above. The relative proportions of olivine and labradorite ($\phi_{olivine}$ and $\phi_{Labradorite}$) were set to 0.001% to make sure that their contribution to the modeled solution composition remains negligible. The flux of exchangeable ions (Ca^{2+}, Mg^{2+}, K^{+}, SO_4^{2-}, HPO_4^{2-}, Al^{3+} et Na^{+}) was defined following a Fickian diffusion law:

$$\frac{dE_{EC}}{dt} = -k_x\left(EC_{surf} - EC_{sol}\right) \quad (8)$$

where E_{EC} is the fraction of sites occupied by an exchangeable ion EC, and k_x is a mass transfer coefficient determined according to the literature (Warfvinge and Sverdrup, 1988). EC_{sol} and EC_{surf} are concentrations calculated in the bulk solution and at the surface of the argilo-humic complex, respectively, based on data from the literature (Alveteg, 1998). Element exchanges between vegetation and soil (F_{veg}) were estimated based on carbon net primary production and carbon recycling determined by the Lund-Potsdam-Jena (LPJ) dynamic global vegetation model (Sitch *et al.*, 2003), and from element/carbon ratios established by Redfield (see Drever *et al.*, 1997). Plant nutrient uptake was allowed down to 1.5 m depth (root compartment), whereas elemental release from litter degradation was only allowed in the superficial soil horizon (above 0.5 m depth) (Beaulieu *et al.*, 2012; Beaulieu *et al.*, 2010; Roelandt *et al.*, 2010). Soil acidification from carbon dioxide partial pressure (p_{CO_2}) induced by autotrophic and

heterotrophic respiration processes were calculated from climatic data (precipitation, temperature, cloud cover, atmospheric CO_2 concentration) sourced from the OHGE and CRU-TS global databases (Harris *et al.*, 2014). The actual chemical composition of the input solutions (throughfall) as a boundary condition at the top of the soil column at each time step was determined using the dynamic version of the code. The model was calibrated using time series from 1987 to 2015 and comparison of the composition of soil solutions collected from the lysimetric plates with those predicted at the corresponding depth (see Tables A.5 and A.6). Sulfate concentration, which only depends on hydrological parameters due to the absence of weatherable sulfate-bearing phases at the Strengbach watershed, were reproduced for the A-horizon (Table A.5). The temperature profile along the soil column was defined for each box by linear interpolation between surface temperature and temperature at 1.5 m-depth, defined at each time step as the gliding annual mean of surface temperatures.

For mineral samples immersed in the Strengbach stream and at the weather station, predicted surface retreats were estimated assuming permanent contact of the mineral with a solution at a pH corresponding to the annual average pH of the stream or of the rainfall, respectively. The solution-mineral interaction was assumed to be constant throughout the incubation period at a temperature corresponding to the annual mean water and air temperature, respectively.

2.6. Bacterial community analysis

2.6.1. DNA extraction

Total DNA was extracted from the soil samples and the stream sediments with a PowerSoil® DNA Isolation Kit (MO BIO, Carlsbad, CA, USA) following manufacturer's instructions. DNA extraction were performed on single samples due to limited quantities of incubated powder. The concentrations of DNA were determined using a Qubit® Fluorometer and Qubit® dsDNA HS

Assay Kit (Invitrogen, Carlsbad, CA, USA). A DNA extraction was first carried out from sterile mineral powder before incubation in the CZ compartment. DNA could not be detected in sterile and cleaned samples. Concentrations of DNA extracted from incubated probes ranged from 0.1 to 2.1 ng.μL^{-1} for the atmospheric probes, 0.6 to >6 ng.μL^{-1} for the A-horizon probes, 0.1 to >6 ng.μL^{-1} for the C-horizon probes, and 3.69 to >6 ng.μL^{-1} for the stream probes.

2.6.2. Illumina MiSeq sequencing and data processing

The sequencing procedure has been described previously (Babcsanyi et al., 2017). Sequencing was performed at the Research and Testing Laboratory (Lubbock, TX, USA) using Illumina MiSeq. The 16S rRNA gene spanning hypervariable region V4 was amplified in a two-step process. Forward primer was based on illumina i5 primer (5'-TCGTCGGCAGCGTCAGATGTGTATAAGAGACAG-3′) the universal bacterial 515F primer (5′-GTGCCAGCMGCCGCGGTAA-3′) (Walters et al., 2011). Corresponding reverse primer was synthesized from illumina i7 primer (5′-GTCTCGTGGGCTCGGAGATGTGTATAAGAGACAG-3′) and universal bacterial primer 806R (5′-GGACTACHVGGGTWTCTAAT-3′). Sequences were generated by nested polymerase chain reaction (PCR) in 25 µL reactors filled up with 1µL of 5 µM primer solution and 1 µL of DNA matrix, diluted in a nucleotide-Taq polymerase-$MgCl_2$ mix.(Qiagen HoStar Taq master mix, Qiagen Inc., Valencia, CA). Reaction was performed in an ABI Veriti incubator (Applied Biosystems, Carlsbad, CA). Reaction products were reamplified by a second PCR step. Primers used in this second step were based on Illumina Nextera sequences: AATGATACGGCGACCACCGAGATCTACAC[i5index]TCGTCGGCAGCGT for the forward and -CAAGCAGAAGACGGCATACGAGAT[i7index]GTCTCGTGGGCTCGG for the reverse. Generated amplicons were visualized with eGels (Life Technology, Grand Island, NY). Products were divided into several equimolar samples and sorted according to their size

by Agencourt AMPure XP (Beckman Coulter, Indianapolis, IN) on a 0.7 ratio basis for each step. DNA concentrations were determined with a Qubit 2.0 spectrofluorometer (Life Technologies, Grand Island, NY) and samples were then loaded in an Illumina MiSeq sequencing device (Illumina Inc., San Diego, CA), equipped with two fluid cells. The data have been deposited with links to BioProject accession number PRJNA492367.

Denoising, chimera checking, generation of operational taxonomic units (OTUs) and taxonomic classification were performed using the custom-scripted bioinformatics pipeline of the Research and Testing Laboratory (Lubbock, TX, USA). Based on the sequence identity percentage derived from BLASTn (Altschul et al., 1990), sequences with identity scores to known or well-characterized 16S rRNA gene sequences >97% identity (<3% divergence) were resolved at the species level, >95% to 97% at the genus level, >90% to 95% at the family level, >80% to 90% at the order level, >80 to 85% at the class level and between 77% – 80% at the phylum level. Any match below this identity level was not used in taxonomical analysis. Matrices of taxonomic data were further used to visualize changes in community composition.

2.6.3. Bacterial diversity and composition analysis

Principal Coordinate Analyses (PCoA) based on Bray-Curtis dissimilarities (Bray and Curtis, 1957; Odum, 1950) was used to visualize ecological gradients underlying the composition of bacterial communities of the environmental probes. PCoA were performed on R software with the vegdist function of the vegan package (Okasen *et al.*, 2016). The relationship between community profiles and the proportion of phylotypes in each sample was investigated by *a posteriori* projection of the genera as weighed average of their contribution to the samples onto the PCoA biplot. Discontinuities within the dataset were revealed by applying a Ward hierarchical clustering (Ward, 1963) as an aggregation rule on Bray-Curtis dissimilarities (Bray and Curtis, 1957; Odum, 1950) with the hclust function of the stats

package. Analysis of similarities (ANOSIM) was used to infer statistical differences between bacterial community clusters ($P < 0.01$) whenever possible. Final clusters were selected on the basis of the corresponding average silhouette width. The significance of the axes in each biplot representation was evaluated following Kaiser-Guttman criterion.

To calculate the diversity and richness indices, the Illumina MiSeq sequences were re-analyzed using MOTHUR version 1.36.1 (http://www.mothur.org) starting from denoised and chimera-checked sequences, aligned, and clustered to define OTUs at 97% sequence identity. Two equivalent datasets were then randomly sub-sampled according to the procedure developed by Schloss *et al* (2009). The resulting datasets were used for rarefaction analysis and to calculate the diversity and richness indices (i.e., Shannon diversity index (H'), inverse Simpson diversity and Chao 1 richness index (S_{chao1}), Babcsanyi *et al.*, 2017).

3. RESULTS

3.1. Soil nutrient pool

Soil physicochemical parameters are provided in Tables A.1-A.4. The profiles of Mg and Ca cationic exchange capacities as a function of depth, which corresponds to inorganic nutrients of interest in the present study, are shown in Fig. 2.

3.2. *In-situ* mineral dissolution rates

Topography measurements on crystals incubated at the Strengbach catchment for 9 and 20 months enabled to estimate the maximal dissolution rates based on surface retreats or roughness (Tables 1 and 2). The surface retreats for olivine ranged from 1 nm (9.38×10^{-13} $mol.m^{-2}.s^{-1}$) to 171 nm (7.17×10^{-11} $mol.m^{-2}.s^{-1}$), both obtained from the meteoric sets of probes (at the weather station). Overall, upper boundaries of reaction rates for olivine were 3.63×10^{-11} $mol.m^{-2}.s^{-1}$

461 (meteoric), 1.20×10^{-11} mol.m^{-2}.s^{-1} (soil A horizon), 1.12×10^{-12} mol.m^{-2}.s^{-1} (soil C horizon) and
462 1.70×10^{-12} mol.m^{-2}.s^{-1} (stream).

463 For labradorite, surface retreats ranged between 1 nm (stream, C horizon) and 5 nm
464 (stream), corresponding to reaction rates ranging from 1.92×10^{-13} to 2.15×10^{-12} mol.m^{-2}.s^{-1}. The
465 average upper boundaries of reaction rates for labradorite were 6.21×10^{-13} mol.m^{-2}.s^{-1}
466 (meteoric), 1.02×10^{-12} mol.m^{-2}.s^{-1} (A horizon), 6.20×10^{-13} mol.m^{-2}.s^{-1} (C horizon) and 1.37×10^{-12} mol.m^{-2}.s^{-1} (stream). Of note, Daval *et al.* (2018) indicated that the measured dissolution rates
468 in the A horizon for labradorite powders incubated for over four years in the same location from
469 2004 to 2008 (1.9×10^{-12} mol.m^{-2}.s^{-1}) are similar to those reported above. For some samples, the
470 surface retreat varied significantly along the boundary of the masks (Fig. 3). In such cases,
471 zones with the greatest surface retreats may coincide with zones of preferential fluid circulation,
472 as indicated by material fragments including colluvium or soil sediments (Fig. 3A and 3C
473 (dashed area) and Fig. 4A and 4C (zone 2)). The surface retreats presented in Tables 1 and 2
474 correspond to zones of maximal surface retreat on the crystals where fluid circulation could be
475 evidenced, unless otherwise specified. In addition to global surface retreats (e.g. red arrow, Fig.
476 5C), local dissolution features were detected (e.g. green arrow, Fig. 5C). These non-geometrical
477 "etch pits" were generally randomly aligned and accounted for locally faster dissolution rates
478 (see red color in Fig. 6B, D and E).

479

480 **3.3. Theoretical mineral reactivity**

481 Dissolution rates of olivine and labradorite in the soil profile were primarily controlled by
482 seasonal temperature variations (for both A- and C-horizons, Fig. 7). Simulated pH values of
483 the A horizon (4.3 ± 0.2) was in agreement with observed values (4.37 ± 0.14), whereas
484 simulated values (5.4 ± 0.2) for the C horizon were slightly higher than those observed (4.83 ±
485 0.07). The simulated solution compositions in the A and C horizons corresponded to far-from-

equilibrium conditions with respect to both labradorite and olivine (i.e., Ω values close to 0 in equation 5). Based on the transition state theory used in the WITCH model (equation 5), such undersaturation states corresponded to dissolution rates that were virtually not affected by the chemical affinity of the system.

For samples from the soil profile, predicted dissolution rates converted into global surface retreats were one to two orders of magnitude greater than rates measured *in-situ* for olivine (Table 2). The laboratory-field discrepancy for dissolution rates in the A horizon varied by a factor of 17 to more than 250 for olivine, and from about 7 to more than 50 for labradorite. In the C horizon, the minimum field-laboratory discrepancy was generally weaker, and ranged from 75 to more than 106 for olivine and from 2 to 7.5 for labradorite.

Regarding the set of probes exposed to the atmosphere, the predicted retreat based on the annual average rainfall properties (pH = 5.4; T = 7.1°C) overestimated the maximal measured retreats by a factor of about 2 for labradorite, and up to a factor of 80 for olivine. Of note, a sample of olivine locally exhibited a retreat of 171 nm, which corresponds to a factor of ~ 1 (no laboratory-field discrepancy).

For samples incubated in the Strengbach stream, theoretical calculations based on the annual average parameters describing water of the Strengbach stream (pH = 6.5; T = 5.8°C) overestimated the measured values by a factor of 9 to 19 for olivine, and a factor of ≥ 1.8 for labradorite.

3.4. Diversification and composition of bacterial communities

3.4.1. General patterns

An average of 33,719 high-quality sequences (>~250 bp) were obtained for each sample by Illumina MiSeq after analysis with Mothur. The OTUs covered 29 phyla, 322 families and 722 genera. Although the sequencing depth (see Fig. A.2 for rarefaction curves) did not

systematically allow for a survey of the full extent of bacterial diversity, rarefaction curves of diversity indices reached asymptotes (Fig. A.2). This indicates sufficient sampling depth to capture the diversity of bacterial communities.

Bacterial community composition of the soil, the weather station and the stream sets significantly differed ($P < 0.01$), irrespective of the incubation time. Sets incubated at the weather station (Fig. 1G) were the richest in Cyanobacteria (> 18%) and in Bacteroidetes (> 22%, Fig. 8), whereas those from the soil (Fig. 1C and D) were enriched in Acidobacteria (>20% horizon 1, > 16%, horizon B). Samples immersed in the stream (Fig. 1J) exhibited a higher mean abundance of Verrucomicrobia.

Differences between compartments of the CZ were also observed at the genus level, in particular amongst taxa potentially involved in mineral weathering processes. For instance, highest proportions of OTUs corresponding to *Geobacter* sp., typical from sedimentary environments and involved in Fe(III) reduction through anaerobic respiration (Esther *et al.*, 2015), were found in the outlet samples. *Aquabacterium* sp. or *Rhodobacter* sp., which encompass several species known for their iron oxidizing capabilities (Hedrich *et al.*, 2011; Weber *et al.*, 2006), were only found in significant proportions in the stream set of probes. Genera known for their ability to weather iron-bearing silicates through siderophore production such as *Sphingomonas* sp. (Calvaruso *et al.*, 2007; Uroz *et al.*, 2009; Uroz *et al.*, 2007), or identified as dissimilatory iron-reducing bacteria (DIRB), such as *Acidiphilium* sp. (Esther *et al.*, 2015) were exclusively found in significant proportions on samples subjected to atmospheric weathering (i.e., at the weather station), especially on olivine samples. Both extracted DNA amounts and diversity indices were larger for the stream sets compared to the soil sets, and generally lower for the sets exposed to the atmosphere (Fig. A.3).

3.4.2. A- and C-horizons soil sets

Bacterial communities of the A horizon differed significantly from those of the C horizon ($P < 0.01$). Taxa potentially involved in mineral alteration appeared to be unevenly distributed between A and C horizons. For example, phylotype sharing 100% similarity with *Mycobacterium kyorinense* strain KUM 060200 16S ribosomal RNA gene, belonging to the genus *Mycobacterium* associated to biotite alteration within the oak mycorhizosphere (Uroz *et al.*, 2009), was only found in litter samples in relative abundance exceeding 0.1 %.

Clustering of samples from both the A and C horizons emphasized distinct communities for mineral probes or environmental matrices (i.e. soil) (Figs. 9 A and 9 C). In the A horizon, bacterial communities from the control empty bags incubated for 9 months, and the quartz samples incubated for 20 months, also differed from the rest of the samples (Fig. 9 D). These samples exhibited lower diversity than other samples from the A horizon, as evidenced by their inverse Simpson (I) and Shannon (H') diversity indices (Fig. A.3 A and B). The richness and bacterial diversity of the olivine sample collected after 20 months of incubation in the A horizon (O20) were higher than for all other samples of the A horizon (Fig. A.3 A and B), and similar to richness and bacterial diversity of corresponding soil sample ($S_{chao1} > 4000$; Fig. A.3 C).

Regarding the C-horizon, bacterial communities changed according to both incubation time (9-month samples *versus* 20-month samples, Fig. 9 A) and mineral type (Fig. 9 A). The bacterial diversity indices associated with labradorite and olivine were the highest ($H' > 5$ and $I > 50$) after 20 months of incubation, and close to those of soil samples. Although diversity was on average lower after 9 months, bacterial diversity for labradorite and olivine was systematically larger than that for quartz. The bacterial diversity for labradorite was higher than that of olivine and quartz, although the bacterial richness for labradorite differed from that of other C horizon samples (Fig. A.3 C).

3.4.3 Weather station

559 Bacterial communities associated with mineral probes exposed to the atmosphere at the
560 weather station were mainly structured according to the mineral type (Fig. 9 A and B). The
561 average bacterial diversity was the lowest among the different sets of this study. The bacterial
562 diversity was the highest for olivine and the lowest for quartz, and significantly increases for
563 olivine between 9 months and 20 months. The olivine sample exhibited the largest specific
564 richness after 20 months of incubation (S_{chao1}> 2000, Fig. A.3).

565 *3.4.4 Stream sets*

566 Bacterial communities from samples immersed in the Strengbach stream differed from
567 those of the related stream sediments (Fig. 9 G). The difference among mineral probes was
568 lower compared to the difference between mineral probes and the stream sediments. Temporal
569 changes in the bacterial communities were observed (Fig. 9 G). The bacterial diversity of
570 environmental probes from the stream was greater than that of probes incubated in other
571 compartments of the CZ (H'> 6.9 and I> 400, Fig. A.3).

572

573 **4. DISCUSSION**

574 Dissolution rates of fresh mineral usually retrieved from laboratory experiments generally
575 differ from rates of mineral aged in the field, due to changes in the mineral surface chemistry
576 over geologic time scales. In addition, the biogeochemical weathering environment of minerals
577 in the critical zone is still largely unknown. In this study, we incubated in the field mineral
578 samples comparable to those used in laboratory experiments to identify *in-situ* (i) hotspots of
579 mineral reactivity in the critical zone, (ii) the extent of the field-lab discrepancy, and (iii) main
580 bacterial patterns associated to mineral surfaces. We discuss below the contribution of intrinsic
581 and extrinsic factors to the field-laboratory discrepancy and factors that may be accounted for
582 to limit this discrepancy. Possible effects of bacterial communities on mineral weathering and

583 the effect of extrinsic factors on mineralosphere development in contrasted compartment of the
584 CZ are specifically addressed.
585
586 **4.1. Contribution of intrinsic and extrinsic factors to the field-laboratory**
587 **discrepancy**
588 Field weathering rates of individual minerals are usually determined with indirect methods.
589 In this study, nanoscale topography variations were used to directly probe mineral dissolution
590 rates in the field (Figs. 5,6 and 10). A major finding is that up to two orders of magnitude
591 separate field measurements and laboratory-based predictions (see Tables 1 and 2) from
592 WITCH. Our *in-situ* measurements confirmed lower field weathering rates determined using
593 indirect methods, although fresh surfaces (laboratory-type samples) were used here. The
594 contribution of intrinsic and extrinsic factors to this discrepancy are discussed below.
595 *4.1.1 Contribution of intrinsic surface aging*
596 Surface aging refers to any physicochemical modification of the surface of an altered
597 silicate contributing to the decline of its dissolution rate. Surface aging has long been suggested
598 to be an intrinsic factor that contributes to the field-lab discrepancy (Daval et al., 2017; Daval
599 et al., 2018; Fischer et al., 2012; Gruber et al., 2014; Lüttge et al., 2013; Nugent et al., 1998;
600 White and Brantley, 2003). We designed the present study to ensure that surface aging was
601 unlikely to significantly affect dissolution rates of probed minerals.
602 Indeed, polished mineral surfaces used to probe *in-situ* dissolution rates of fresh silicate
603 surfaces in the field minimized the contribution of intrinsic factors to the field-laboratory
604 discrepancy. Assuming that aging (and the possible formation of passivation layers) requires a
605 minimal portion of mineral surface to be weathered (in agreement with recent studies such as
606 Gin et al. (2015) or Daval et al. (2018)), the reaction progress (ξ) after which it becomes
607 significant (i.e., beyond the uncertainties of the measurement), should be specific to the

608 considered mineral at given conditions. Reaction progress (ξ) quantifies here the extent of the
609 reaction of dissolution (in mol.m^{-2}) for either olivine or labradorite. In a recent study, Wild *et*
610 *al.* (2016) reported that the decline of labradorite dissolution rate related to surface ageing was
611 observed for $\xi \geq 2.54\times10^{-3}$ mol.m^{-2}. Regarding olivine, mineral ageing was evidenced in
612 laboratory conditions for $\xi \geq 6.92\ 10^{-2}$ mol.m^{-2} (Daval *et al.*, 2011). As reported in Tables 1 and
613 2, the maximum reaction progress expected for labradorite and olivine, calculated as the product
614 of the dissolution rate times the incubation period, reached $\xi = 5.68\ 10^{-4}$ mol.m^{-2} (labradorite
615 altered into the A horizon over 20 months) and $\xi = 1.71\ 10^{-2}$ mol.m^{-2} (olivine altered into the A
616 horizon over 20 months), respectively, which are below the threshold limit reported above.
617 Hence, any difference between the measured and the modeled reaction rates can be attributed
618 to extrinsic factors. In addition, fresh labradorite powders incubated in the A horizon of the
619 exact same plot for durations exceeding four years were still far from being completely covered
620 with passivating surface layers (Daval et al., 2018), thereby further supporting this assertion.
621 *In-situ* measurements could thus be directly compared with WITCH simulations that rely on
622 kinetic rate laws obtained from laboratory experiments.
623
624 *4.1.2 Extrinsic factors in the laboratory-field discrepancy*
625 Dissolution rates depend on extrinsic parameters, as emphasized in the simplified version
626 of equation 5, adapted from (Lasaga, 1998):

$$R_{min} = A.\,exp\left(\frac{-E^{i}_{a,min}}{RT}\right).\,a^{n}_{H^+}.\,f(\Delta G_{r,sil}), \quad (9)$$

627 describing mineral weathering rate R_{min} as a function of temperature T, the Gibbs free energy
628 with respect to silicate (sil) dissolution $\Delta G_{r,sil}$, and the pH of the fluid, quantified by the
629 chemical activity of protons ($a^{n}_{H^+}$). These three parameters are the main extrinsic factors that
630 control the aqueous mineral dissolution rate. Aside from the gas constant R, the other
631 parameters of this equation, such as the Arrhenius pre-exponential factor A, the activation

energy $E^{i}_{a,min}$, and the reaction order n are constants derived from laboratory experiments, which are specific to the considered dissolution reaction.

A wide range of values has been reported for each of these three parameters, even for the same mineral (Palandri and Kharaka, 2004). Such disparities in parameter values can lead to significant uncertainties between predicted mineral dissolutions rates (Rimstidt *et al.*, 2012). Parameters chosen for the present study were retrieved from Rosso and Rimstidt (2000) data for olivine (A = 3.467 mol.m^{-2}.s^{-1}, E_a = 42.6 kJ.mol^{-1}, and n = 0.50) and Palandri and Kharaka (2004) data for labradorite (A = 0.321 mol.m^{-2}.s^{-1}, E_a = 42.1 kJ.mol^{-1}, and n = 0.63). These two studies provide a meta-analysis of experimental kinetic data and apply statistical methods to infer the rate parameters reported above. We verified that the corresponding rate laws satisfactorily predict dissolution rates of the labradorite and olivine powders reacted in mixed flow set-ups, using the soil solutions collected from lysimetric plates at the Strengbach catchment (see details in Wild et al. (2018)).

As temperature is an input parameter of the numerical simulations, it can be ruled out as a factor explaining the field-laboratory discrepancy. Since simulated pH values were either similar to those measured, or slightly higher, the contribution of this parameter to the minimal field-lab discrepancy reported in Tables 1 and 2 is negligible. Hence, the observed field-laboratory discrepancy can be ascribed either to the effect of $\Delta G_{r,sil}$ quantified by the $f(\Delta G_{r,sil})$ function, or to the fluid-mineral contact time, which is an implicit condition to equation 9.

Surface retreats could only be distinguished in areas where fluid circulation occurred on labradorite and olivine samples (see section 3.2 and Figs. 3 and 4, respectively). This indicates that the temporal and spatial extents of fluid-mineral contact may partly account for the field-laboratory discrepancy. In terms of spatial extent of the fluid-mineral interface, no compact coating of secondary minerals potentially masking significant portion of mineral surface could be observed on mineral surfaces after incubation. This hypothesis was therefore ruled out.

The extent of fluid-mineral contact time parameter is, on the other hand, indirectly implemented in WITCH with the soil moisture saturation factor (SMS) given in equation 4. SMS estimates the proportion of the bulk soil volume saturated with aqueous solution for a given depth, which corresponds to the proportion of minerals that is susceptible to exchange matter with the fluid. However, the SMS does not allow to localize fluid circulation zones at the soil profile scale. The discrepancy between the data and the model (Fig. 11) is unlikely to result from the hydrological budget alone since the concentration of conservative tracers, such as sulfate anions, fitted observation for the A-horizon (see section 2.5 and Table A.5). Indeed, surface retreats measured for mineral probes of the stream sets were at best one order of magnitude lower than those estimated with kinetic rate laws derived from laboratory experiments, despite permanent fluid-mineral contact (Tables 1 and 2).

Finally, the effect of the Gibbs free energy of reaction on mineral dissolution rate may contribute to explain the field-lab discrepancy. The dependence of mineral dissolution rate on $\Delta G_{r,sil}$ is implemented in WITCH through the $(1 - \Omega)$ term in equation 5, in agreement with the transition state theory (TST), which is equivalent to:

$$f_1(\Delta G_r) = 1 - \left[\exp\left(\frac{\Delta G_r}{RT}\right)\right]^S \quad (10)$$

in equation (9). Even though this relation is widely used in reactive transport codes and sometimes successfully applied to reproduce field observations (Goddéris and Donnadieu, 2009; Godderis et al., 2006; Violette et al., 2010), it may not be appropriate to describe complex reaction pathways (Gin *et al.*, 2008). For instance, the sum of two parallel reactions, with a transition from far-to-equilibrium to close-to-equilibrium dissolution regime occurring at ΔG_r = -7.5 kcal.mol^{-1}, better described the dissolution kinetics of labradorite (Taylor *et al.*, 2000). To test the effect of the selection of the $f(\Delta G_{r,sil})$ function, the empirical relation of Taylor *et al.* (2000) was implemented in WITCH:

$$f_2(\Delta G_r) = \left\{ \begin{array}{c} 0.76 * \left[1 - exp\left(-1.3 * 10^{-17} * \left(\frac{|\Delta G_r|}{RT}\right)^{14}\right)\right] \\ +0.24 * \left[1 - exp\left(-0.35 * \frac{|\Delta G_r|}{RT}\right)\right] \end{array} \right\} \quad (11)$$

with the exception of a minor sign correction (the original paper mistakenly indicates -0.24 instead of +0.24 for eq. 11). Variations of the f_1 and f_2 functions for the A and C horizons are shown in Fig. 11 A. $\Delta G_{r,sil}$ did not affect labradorite dissolution rate in the soil profile if one considers the f_1 function. In contrast, a significant decrease of the apparent dissolution rate of labradorite in the C horizon occurred using the f_2 function. Regarding the C horizon, changing the $f(\Delta G_{r,sil})$ function for the f_2 function totally resolved the field-laboratory discrepancy for labradorite, as shown by values of $\Delta_{L/F} < 1$ (parenthesis, Table 1) and in agreement with Gruber *et al.*, 2014. For the A-horizon, however, the field-laboratory discrepancy could not be totally explained by the equilibrium term since the discrepancy persisted ($\Delta_{L/F} > 1$). Regarding olivine, in the absence of an alternative function describing the $R_{min} - \Delta G_{r,sil}$ dependence of its dissolution kinetics, the TST-based relation was used by default, although it may not be fully relevant.

Overall, this shows that current models may partly fail to capture the effects of both heterogeneity of fluid circulations and local physicochemical conditions on mineral dissolution rates in soils of the CZ. The presence of microorganisms associated to minerals may be one of the factors influencing both fluid circulation and local physicochemical conditions. The relationship between bacterial communities and minerals in various compartments of the CZ is discussed below.

4.2. Effect of microorganisms on mineral weathering in the CZ

Amongst other extrinsic parameters, biota has been shown to affect mineral weathering (Ahmed and Holmstrom, 2015; Bonneville *et al.*, 2009; Courty *et al.*, 2010; Li *et al.*, 2016;

Uroz *et al.*, 2009). Most strikingly, the weathering rate for the olivine surface incubated for 9 months at the weather station were low, corresponding to a retreat < 1 nm (Table 2), whereas the surface incubated for 20 months exhibited an exceptional retreat of up to 172 nm (Fig. 10), corresponding to a field-laboratory discrepancy value of $\Delta_{L/F} = 1$ (no discrepancy, see Table 2). Rainwater cannot be considered as the unique weathering agent for olivine because open-air incubation conditions offer rather homogeneous input weathering conditions. Variations of reaction rates are at odds with the exposure of olivine surface to homogeneous reactive fluids at the weather station. In addition, the mineral surface retreat measured after 20 months would virtually corresponds to a permanent interaction of the mineral with a fluid of average composition of the rainwater. This condition is unlikely as the samples incubated at the weather stations were prone to drying-wetting cycles. In addition, permanent fluid interaction is inconsistent with the retreat observed after 9 months of incubation in the same conditions (sample MO9, Table 2). The occurrence of several microorganisms on the meteoric probes supports the hypothesis that organisms contributed to mineral weathering.

Microorganisms can also affect locally fluid circulation in soil (Or *et al.*, 2007), which can impact mineral weathering by regulating fluid-mineral contact. More specifically, biofilms can disrupt interactions between mineral surface and bulk fluid and stabilize locally zones of preferential fluid circulation. Here, samples from the A-horizon show that the flow path of the solution can be precisely constrained around the fluid boundary (± 10 μm, approximate width of the transition zone indicated by dashed lines in Fig. 4G) (Fig. 4D-F). Biofilms may thus subtly control fluid flow and act similarly to the RTV glue used to estimate global surface retreat (dark grey area, Fig. 4C and striped area, Fig. 4D-F and 4H).

While biofilm may have increased the dissolution rate of olivine exposed to meteoric fluid or indirectly contributed to the field-lab discrepancy by affecting fluid-mineral contact, direct observation of mineral-microorganism contact is missing to support such hypothesis.

Concerning soil compartments, no clear direct evidence of bacterial weathering could be observed despite biological weathering could have been favored by K, Ca and Mg concentrations typical for nutrient-poor pedological systems (van der Heijden *et al.*, 2013). Mg concentrations in the soil profile (Fig. 2) were similar to those observed in a reference forest plot located in the Morvan Mountains (Burgundy, France), which exhibited Mg-deficiency thirty years after clear-cutting native forest (van der Heijden *et al.*, 2013). Moreover, symptoms of forest decline, and Mg and Ca nutritional deficits in trees were already described at the Strengbach catchment (Dambrine *et al.*, 1992). We thus tried to indirectly probe clues possible mineral-bacteria interactions by tracking the development of mineral-specific bacterial communities, and how their composition varied according to the mineral substrates (Jones and Bennett, 2014) or their dissolution rates (Uroz *et al.*, 2012). The influence of minerals on bacterial communities in their direct vicinity and the potential for mineral weathering of bacterial phylotypes found in the environmental probe are discussed below. However, one has to keep in mind that only about 6% of the bacterial phyla are identified by usual taxonomic databases (Solden *et al.*, 2016; Yarza *et al.*, 2014). Therefore, relating weathering fluxes to specific bioweathering bacteria in the field solely based on their phylogenetic affiliation remains an elusive goal. In this exploratory study, the relevance of bacterial diversity as a potential indicator of the mineral-bacteria interactions was evaluated.

4.2.1 Establishment of mineral-specific bacterial communities

Our results are consistents with the hypothesis that incubated minerals host specific mineralosphere bacterial communities. Indeed, mineralosphere bacterial communities from the soil profile or the Strengbach stream differed from those of the corresponding bulk soil or stream sediment samples respectively. Similarly, mineral-specific communities from the meteoric sets established according to the mineral type. This is in agreement with previous

752 results obtained with a similar approach using *in-situ* incubation of fresh minerals (Mitchell *et*
753 *al.*, 2013; Uroz *et al.*, 2012), field samples (Gleeson *et al.*, 2006), or microcosms inoculated
754 with microbial consortia from a forest soil (Heckman *et al.*, 2013). This point is highlighted
755 here since the development of mineral-specific bacterial communities may reflect the
756 development of phylotypes adapted to mineral weathering, along with the development of
757 bioweathering processes adapted to the mineral substrate.

758 Interestingly, our results also show that mineralosphere communities changed over time.
759 While previous studies provided "snapshots" of mineralosphere bacterial communities
760 (Mitchell et al., 2013; Uroz et al., 2012), two incubation times were considered in the present
761 approach (9 and 20 months), which constitutes an attempt to address temporal changes of
762 bacterial communities. In the C soil horizon and stream sets of probes, time rather than intrinsic
763 mineral weatherability seemed to constitute a primary factor driving community composition
764 (Fig. 9 E). In probes from the C horizon, bacterial communities associated with olivine and
765 labradorite differed more from those associated with non-reactive samples (quartz) after 20
766 months of incubation than in the initial stages of the mineralosphere formation (i.e., after 9
767 months). This support the idea that the mineralosphere develops according to mineral reactivity
768 under field conditions, even though more probes and replicates in each CZ compartments are
769 necessary to confirm this trend.

770

771 *4.2.2. Influence of extrinsic factors on mineralosphere development*

772 Comparison of environmental probes incubated in the atmospheric, soil and stream
773 compartments of the CZ revealed the effect of extrinsic factors (i.e., not related to the mineral)
774 on mineralosphere bacterial communities. Altogether, the results suggest that the relative
775 contribution of extrinsic *versus* intrinsic factors on the differentiation of bacterial communities

776 increases across CZ compartments, following a meteoric < C-horizon < A-horizon < stream
777 pattern.

778 The meteoric sets of probes were exclusively exposed to atmospheric inputs, which are
779 intermittent and nutrient-poor compared to those recorded in the soil or in the stream. In soils,
780 the hygrometry and cationic inputs may be buffered by secondary mineral phases. By contrast,
781 the composition of the fluid in direct contact with mineral probes in the stream was rapidly
782 controlled by the stream hydrochemistry. In the case of the meteoric sets of probes, the mineral
783 type was expected to largely control the surface environment, and thus the response of bacterial
784 communities. Indeed, the mineral represented the main source of inorganic nutrients and/or
785 toxic elements, such as Al (Jones and Bennett, 2014; Singh et al., 2005). Lower overall bacterial
786 diversity for the meteoric sets of probes compared to other sets, and distinct bacterial
787 communities (Fig. 9 A) and diversity (Fig. A.3) according to the mineral substrate, support this
788 hypothesis. The lower impact of external inputs in the case of meteoric probes may also explain
789 the rapid differentiation of bacterial communities according to the mineral type, regardless of
790 the incubation time.

791 Contrasting with observations from the C horizon and meteoric sets of probes, bacterial
792 communities from the A horizon did not cluster according to mineral type. This may reflect
793 more dynamic conditions in the A horizon with respect to both physicochemical conditions and
794 microbial diversity. This is suggested by heterogeneous flows that were evidenced on the probe
795 surface (Fig. 3 and Fig. 4). In addition, organic matter cycling and bioturbation (Gutiérrez and
796 Jones, 2006) may particularly affect, on the short-term, microorganisms of the A horizon by
797 altering nutrient inputs or physicochemical parameters. This may tremendously confound and
798 delay the response of microbial communities to mineral reactivity.

799 The effect of extrinsic factors was apparently even stronger in the case of the stream probes
800 because fluid circulation directly and continuously impacted the physicochemical

characteristics of the incubation environment (T, pH, etc.). This is emphasized by the similar composition of bacterial communities observed amongst samples in the stream set of probes (Fig. 9 H) and the higher bacterial diversity observed on these samples compared to other compartments (Fig. A.3). In this case, continuous inputs of dissolved nutrients and particle-associated biomass (Fig. 1 J) may interfere with the development of the mineralosphere. This may in turn challenge and delay the detection of a mineralosphere effect (i.e., specific bacterial communities associated to specific minerals). Analogous effects were observed in an oceanic context, where minerals incubated close to hydrothermal discharge (providing a continuous input of nutrient from fluids) only served as a solid support on which bacteria could attach, whereas similar minerals located far from these fluids inputs served as Fe source for microorganisms (Henri et al., 2016). As a result, the effect of extrinsic factors on the differentiation of mineralosphere bacterial communities may largely differ among CZ compartments for similar incubation times.

4.2.3. Occurrence of potential mineral-weathering bacteria

Potential mineral-weathering bacterial taxa found in the environmental probes included *Pseudomonas* sp., *Collimonas* sp., *Burkholderia* sp., *Janthinobacterium* sp., *Leifsonia* sp., and *Arthrobacter* sp. The occurrence of these taxa underscores the potential for biotic alteration in the mineralospheres of the investigated soils. These taxa were found in higher abundance not only in the sets of probes incubated in the soil profile compared to other compartments (2.1% vs. 0.1% on average, Fig. 12), but also in the mineralosphere compared to the corresponding bulk soil horizons (2.6% vs. 0.2% on average, Fig. 12).

Pseudomonas sp. dominated the studied mineralospheres, with an average proportion of 2.5% for the whole dataset and of 4.5% in the soil samples (< 0.1% for the other compartments of the critical zone). Phylotypes belonging to the *Pseudomonas* genus have been described in

826 the literature for their ability to dissolve biotite (Uroz *et al.*, 2009). For both the A and C
827 horizons of the soil profile, *Pseudomonas* sp. was more abundant on labradorite and olivine
828 samples. The proportion of *Pseudomonas* sp. remained constant over time in samples from the
829 C horizon, whereas it decreased in the A horizon between 9 and 20 months of incubation (Fig.
830 12). This suggests that *Pseudomonas* sp. pioneered the colonization of the mineral probes of
831 the soil sets, and mainly occurred in relation to saprolitic alteration. This may be due to the
832 significance of rock weathering in the C horizon relative to other processes that may affect
833 microbial assemblages in the A horizon (e.g. bioturbation, degradation of organic matter or
834 nutrient cycling).

835 *Collimonas* sp. was also particularly abundant in the soil mineral probes (1.9%) compared
836 to other compartments (< 0.1%). It has long been thought that species belonging to the
837 *Collimonas* genus were bacteria living at the expense of organic exudates produced by fungi of
838 the mycorrhizosphere (de Boer *et al.*, 2004). However, *Collimonas* sp. are also capable of
839 extracting elements, such as iron from biotite (Calvaruso *et al.*, 2007; Uroz *et al.*, 2007), or
840 from granite powders (Lapanje *et al.*, 2012) by the production of siderophores, thus supplying
841 their fungal hosts with inorganic nutrients. In our samples, *Collimonas* sp. was found in a larger
842 proportion in the C horizon (i.e., in contact with the saprolite) than in the organic-rich A
843 horizon.

844 The projection of *Collimonas* sp. found for each of the corresponding PCoA analyses (Fig.
845 9) revealed similar trends for samples from the two soil horizons. *Collimonas* sp. prevailed on
846 quartz and labradorite after 9 months of incubation, whereas it decreases in all samples between
847 9 and 20 months, except for olivine, where it increases over the same period. The decline of
848 *Collimonas* sp. was associated to increasing bacterial diversity in all sets of probes incubated
849 in the soil, except for quartz in the A horizon (Fig. A.3). This suggests that *Collimonas* sp. may

first establish at the fungus-rock interface, before specializing in iron extraction through the production of siderophores.

In average, *Burkholderia* sp. accounted for 1.0% of the total genera recovered from the probes. *Burkholderia* sp. have been reported to enhance the dissolution of biotite, like some members of the genus *Collimonas* (Calvaruso *et al.*, 2007; Uroz *et al.*, 2007), but also apatite (Lepleux *et al.*, 2012; Mailloux *et al.*, 2009), phosphate minerals (Kim *et al.*, 2005; Vassilev *et al.*, 2006), quartz (Ullman *et al.*, 1996), bytownite (Barker *et al.*, 1998; Welch *et al.*, 1999) and other feldspars (Ullman *et al.*, 1996), and more generally granite (Wu *et al.*, 2008) or basalt (Wu *et al.*, 2007). Similarly to *Collimonas* sp., *Burkholderia* sp. was mainly found in soil compartments, especially in the A horizon, in particular associated to the quartz sample incubated for 20 months. The latter sample also exhibits a notably low bacterial diversity (H'<5 and I <50, Fig. A.3). *Burkholderia* sp. therefore seems to correspond to "lithophilic" bacteria particularly adapted to the context of the A horizon.

Janthinobacterium sp., *Leifsonia* sp. and *Arthrobacter* sp., which have been described for their ability to dissolve granite through the production of oxalic acid and hydrogen cyanide (Frey *et al.*, 2010), also belonged to the first decile of most abundant bacterial genera. Biotite dissolution was enhanced by species of the genus *Janthinobacterium* (Uroz *et al.*, 2009). Species belonging to the genus *Arthrobacter* may promote the dissolution of hornblende (Kalinowski *et al.*, 2000), quartz and feldspars (Ullman *et al.*, 1996), including bytownite (Barker *et al.*, 1998; Welch *et al.*, 1999). The proportions of *Leifsonia* sp. and *Arthrobacter* sp. after 9 months was higher in the C horizon compared to the A horizon, whereas the proportions were larger in quartz samples after 20 months in both soil horizons (Fig. 12). *Leifsonia* sp., or *Arthrobacter* sp. may preferentially adapt to environments with a lower influence of extrinsic factors, like in the C horizon compared to the A horizon (see section 4.2.2 and Fig. 12), or to the quartz surface, not releasing any toxic or valuable elements. This results in high apparent

proportion for the samples associated to low diversity, such as the quartz samples. *Janthinobacterium* sp. occurred in a larger proportion in probes from the C horizon, in particular on olivine and labradorite probes that bear elements of interest such as Mg, Fe or Ca (Fig. 12). The population decrease between 9 and 20 months of incubation suggests that *Janthinobacterium* sp. may be "lithophilic" and compete with other bacterial processes, as described above.

Finally, *Polaromonas* sp., which was previously reported in the context of granite weathering (Frey *et al.*, 2010), was present in high proportions in all sets of probes of the C horizon.

Overall, bacterial communities of mineralosphere of the soil profile feature several populations that may be involved in mineral weathering. The distribution of bacterial taxa putatively associated with mineral weathering coincided with the disturbed bacterial pattern of the A horizon. Indeed, extrinsic factors (i.e. factors influencing the bacterial community that are not related to the mineral substrate) may considerably affect the distribution of the taxa potential associated with mineral weathering, such as *Pseudomonas* sp., *Janthinobacterium* sp., *Leifsonia* sp., or *Arthrobacter* sp. Such disturbances may delay the development of a mineralosphere specific to the mineral type.

4.2.4 Do bacteria with weathering ability actively dissolve minerals?

Determining whether microorganisms with known weathering activity and present at the surface of minerals actively contribute to mineral dissolution remains challenging. While to date most of the evidences of bacterial mineral dissolution have been based on microscopic observations (Bennett *et al.*, 2001; Jongmans *et al.*, 1997), this approach is still controversial (Benzerara *et al.*, 2007). Another methodology has been suggested, which considers a linear relationship between *in-situ* weathering rates and bacterial diversity (Uroz *et al.*, 2012). In our

case, however, no clear correlation could be established between the extent of mineral weathering and bacterial diversity or enrichment of specific taxa (i.e., *Collimonas* sp., *Burkholderia* sp., *Pseudomonas* sp., *Janthinobacterium* sp., *Leifsonia* sp., or *Arthrobacter* sp.). However, these specific taxa, which may be functionally related to mineral weathering, do not necessarily express this function, and their occurrence may not necessarily reflect a selective pressure for their bioweathering ability.

Nevertheless, regarding samples exposed to open-air weathering at the weather station, bacterial diversity globally increases with increasing mineral weatherability (quartz < labradorite < olivine), irrespective of the mineral incubation time. This supports the clustering of bacterial communities according to the mineral substrate shown in Fig. 9 A. In the A-horizon, the Shannon and inverse Simpson diversity indices are higher for olivine (the most weatherable mineral) incubated 20 months in the A horizon than for all the other mineral samples of this compartment (Fig. A.3). The potential for nutrient mobilization of a given mineral may thus stimulate competition between bioweathering agents and support the development of diverse bacterial communities.

Regarding the C horizon, variation in the diversity indices echoes the cluster analysis (Fig. 9 E). This stresses the first-order importance of time on the composition of bacterial communities: time prevailed over the type of the mineral in the C horizon. Globally, diversity increased for all three minerals as a function of time. On the other hand, diversity was significantly higher for "reactive" minerals after 20 months of incubation and reached that of the corresponding soil samples (Fig. A.3 A, B). Bacterial richness (Chao 1 index) was only significantly higher for labradorite after 20 months, which reflected the diversification of bacterial communities in the C horizon for minerals. The low differences of bacterial diversity between mineral samples immersed in the Strengbach stream confirms the second-order role played by mineral substrates for this compartment.

To conclude, diversity analysis of bacterial communities for samples incubated in the A and C horizons of the soil profile and at the weather station suggests a relationship between microbial community diversity and mineral reactivity. Our results support the hypothesis that mineral substrates, depending on their incubation context, may affect microbial communities in their mineralospheres. Diversity analysis of bacterial communities suggests that potential bioweathering bacteria of the A horizon are preferentially associated to (Mg, Fe)-bearing phases, such as olivine, whereas those of the C horizon are rather associated to feldspars minerals, such as labradorite. However, this study is not fully conclusive as to whether the potential of bacterial weathering is actually expressed. This would require strengthening the statistical significance of the results by increasing the number of probes and replicates on the one hand, and to statistically relate dissolution features to bioweathering processes. To address this issue, future studies may consider imaging spatial distribution of microorganisms on mineral samples, especially by assessing their distance from the surface or from dissolution "hot spots" with confocal laser scanning microscopy. Once microorganisms are located on the mineral surface, possible associated dissolution features of biotic origin may be used to quantify associated "biotic rates" by rate spectra analysis (Fischer et al., 2012), such as that presented on Fig. 6.

5. SUMMARY AND CONCLUSIONS

The present study shows that *in-situ* mineral dissolution rates and bioweathering environments of minerals can be directly probed *in-situ* in contrasted compartments of the CZ. This approach is complementary to those already used to estimate mineral weathering rates in the field, as it allows for the estimation of mineral weathering rates over short timescales (from months to years).

In spite of the limited number of samples that could be incubated, fundamental parameters to understand mineral dissolution in the CZ were identified. In particular, extrinsic factors may partly explain the gap existing between estimates of silicate dissolution rates obtained in the laboratory and in the field, while potential bioweathering bacteria were found in all CZ compartments. Salient results of the present study can be summarized as follows:

1) In A and C soil horizons, simulated dissolution rates converted into global surface retreats were greater by a factor of 1 to 270 for olivine, and of 2 to 54 for labradorite than those measured *in-situ*.
2) The heterogeneity of fluid circulation in soil profiles should be accounted for in chemical weathering models as it can significantly affect *in-situ* mineral weathering rates.
3) The effect of the Gibbs free energy of reaction on labradorite dissolution rates partly explains the discrepancy between laboratory estimates and field measurements for the A and C soil horizons.
4) The nature of the mineral substrate affects bacterial communities of the mineralosphere. This process can however be affected or delayed by extrinsic factors, such as nutrient or biomass inputs mediated by fluid circulation.

In parallel, our study also raised some issues that need to be explored in the future. Although potential bioweathering bacterial phylotypes were detected on environmental probes incubated in A and C horizons, bioweathering activities could not be proved, and the contribution of bacterial activities to the total weathering flux could not be quantified. The approach proposed in this study may however be generalized to evaluate *in-situ* expression of microbial bioweathering functions (i) to quantify the effect of microbial communities on mineral

dissolution rate, and (ii) to gradually include bacteria/mineral interactions in next-generation chemical weathering models.

Finally, incubation of a greater number of integrative reactivity probes of various mineral types may help in the future to unravel effective local reaction conditions controlling *in-situ* mineral reactivity in CZ compartments.

6. ACKNOWLEDGEMENT

The making of probes and of the experimental setup beneficiated from the technical support of Lisa Wild and René Wild that are warmly acknowledged. The follow up of the experiment would have not been possible without the help of the OHGE team, and particularly Solenn Cotel and Sylvain Benarioumlil. Authors also wish to thank Michael Heap, Helline Maison and Gilles Morvan for technical assistance and François Guyot for numerous and fruitful discussions that contributed to this manuscript. This work was funded through a grant to Gwenaël Imfeld for the project MicXtreme under the framework of the LabEx G-EAU-THERMIE PROFONDE project ANR-11-LABX-0050, and through a grant to Damien Daval under the framework of the VALVE project (EC2CO-BIOHEFECT program coordinated by the CNRS–Institut National des Sciences de l'Univers).

7. REFERENCES CITED

997 Ackerer, J., Chabaux, F., Van der Woerd, J., Viville, D., Pelt, E., Kali, E., Lerouge, C.,
998 Ackerer, P., Roupert, R.D., Negrel, P., 2016. Regolith evolution on the millennial timescale
999 from combined U-Th-Ra isotopes and in situ cosmogenic Be-10 analysis in a weathering profile
1000 (Strengbach catchment, France). Earth Planet. Sci. Lett.453, 33-43.
1001 Ahmed, E., Holmstrom, S.J.M., 2015. Microbe-mineral interactions: The impact of surface
1002 attachment on mineral weathering and element selectivity by microorganisms. Chem. Geol.
1003 403, 13-23.
1004 Alisa Mast, M., Drever, J.I., 1987. The effect of oxalate on the dissolution rates of oligoclase
1005 and tremolite. Geochim. Cosmochim. Acta 51, 2559-2568.
1006 Altschul, S.F., Gish, W., Miller, W., Myers, E.W., Lipman, D.J., 1990. Basic local
1007 alignment search tool. J. Mol. Biol. 215, 403-410.
1008 Alveteg, M., 1998. Dynamics of forest soil chemistry. Ph.D, Lund University.
1009 Arvidson, R.S., Ertan, I.E., Amonette, J.E., Luttge, A., 2003. Variation in calcite dissolution
1010 rates: A fundamental problem? Geochim. Cosmochim. Acta 67, 1623-1634.
1011 Arvidson, R.S., Luttge, A., 2010. Mineral dissolution kinetics as a function of distance from
1012 equilibrium - New experimental results. Chem. Geol. 269, 79-88.
1013 Augusto, L., Turpault, M.P., Ranger, J., 2000. Impact of forest tree species on feldspar
1014 weathering rates. Geoderma 96, 215-237.
1015 Babcsanyi, I., Meite, F., Imfeld, G., 2017. Biogeochemical gradients and microbial
1016 communities in Winogradsky columns established with polluted wetland sediments. FEMS
1017 Microbiol. Ecol.93.
1018 Barker, W.W., Banfield, J.F., 1996. Biologically versus inorganically mediated weathering
1019 reactions: Relationships between minerals and extracellular microbial polymers in lithobiontic
1020 communities. Chem. Geol. 132, 55-69.

1021 Barker, W.W., Welch, S.A., Chu, S., Banfield, J.F., 1998. Experimental observations of the
1022 effects of bacteria on aluminosilicate weathering. Am. Miner. 83, 1551-1563.
1023 Beaulieu, E., Godderis, Y., Donnadieu, Y., Labat, D., Roelandt, C., 2012. High sensitivity
1024 of the continental-weathering carbon dioxide sink to future climate change. Nat. Clim. Change.
1025 2, 346-349.
1026 Beaulieu, E., Godderis, Y., Labat, D., Roelandt, C., Oliva, P., Guerrero, B., 2010. Impact
1027 of atmospheric CO_2 levels on continental silicate weathering. Geochim. Cosmochim. Acta 74,
1028 A65-A65.
1029 Beig, M.S., Luttge, A., 2006. Albite dissolution kinetics as a function of distance from
1030 equilibrium: Implications for natural feldspar weathering. Geochim. Cosmochim. Acta 70,
1031 1402-1420.
1032 Bennett, P.C., Hiebert, F.K., Choi, W.J., 1996. Microbial colonization and weathering of
1033 silicates in a petroleum-contaminated groundwater. Chem. Geol. 132, 45-53.
1034 Bennett, P.C., Rogers, J.R., Choi, W.J., 2001. Silicates, silicate weathering, and Microb.
1035 Ecol.. Geomicrobiol. J. 18, 3-19.
1036 Benzerara, K., Menguy, N., Banerjee, N.R., Tyliszczak, T., Brown, G.E., Guyot, F., 2007.
1037 Alteration of submarine basaltic glass from the Ontong Java Plateau: A STXM and TEM study.
1038 Earth Planet. Sci. Lett.260, 187-200.
1039 Bonneau, M., Dambrine, E., Nys, C., Range, r.J., 1991. Apports acides et cycles des cations
1040 et de l'azote : quelques reflexions à partir des dispositifs de Monthermé (Ardennes) et d'Aubure
1041 (Vosges). Sci. du Sol 29, 125-145.
1042 Bonneville, S., Bray, A.W., Benning, L.G., 2016. Structural Fe(II) oxidation in biotite by
1043 an ectomycorrhizal fungi drives mechanical forcing. Environ. Sci. Technol. 50, 5589-5596.

Bonneville, S., Smits, M.M., Brown, A., Harrington, J., Leake, J.R., Brydson, R., Benning, L.G., 2009. Plant-driven fungal weathering: Early stages of mineral alteration at the nanometer scale. Geology 37, 615-618.

Brantley, S.L., Liermann, L., Bau, M., Wu, S., 2001. Uptake of trace metals and rare earth elements from hornblende by a soil bacterium. Geomicrobiol. J.18, 37-61.

Bray, R.J., Curtis, J.T., 1957. An ordination of the upland forest communities in southern Wisconsin. Ecol. Monogr. 27, 325-349.

Calvaruso, C., Turpault, M.-P., Leclerc, E., Frey-Klett, P., 2007. Impact of ectomycorrhizosphere on the functional diversity of soil bacterial and fungal communities from a forest stand in relation to nutrient mobilization processes. Microb. Ecol. 54, 567-577.

Carroll, S.A., Knauss, K.G., 2005. Dependence of labradorite dissolution kinetics on CO_2(aq), Al(aq), and temperature. Chem. Geol. 217, 213-225.

Courty, P.E., Buee, M., Diedhiou, A.G., Frey-Klett, P., Le Tacon, F., Rineau, F., Turpault, M.P., Uroz, S., Garbaye, J., 2010. The role of ectomycorrhizal communities in forest ecosystem processes: New perspectives and emerging concepts. Soil Biol. Biochem. 42, 679-698.

Dambrine, E., Carisey, N., Pollier, B., Granier, A., 1992. Effects of drought on the yellowing status and the dynamic of mineral elements in the xylem sap of a declining spruce stand (Picea abies Karst.). Plant Soil 150, 303-306.

Daval, D., Bernard, S., Rémusat, L., Wild, B., Guyot, F., Micha, J.S., Rieutord, F., Magnin, V., Fernandez-Martinez, A., 2017. Dynamics of altered surface layer formation on dissolving silicates. Geochim. Cosmochim. Acta 209, 51-69.

Daval, D., Calvaruso, C., Guyot, F., Turpault, M.-P., 2018. Time-dependent feldspar dissolution rates resulting from surface passivation: Experimental evidence and geochemical implications. Earth Planet. Sci. Lett.498, 226-236.

Daval, D., Hellmann, R., Saldi, G.D., Wirth, R., Knauss, K.G., 2013. Linking nm-scale measurements of the anisotropy of silicate surface reactivity to macroscopic dissolution rate laws: New insights based on diopside. Geochim. Cosmochim. Acta 107, 121-134.

Daval, D., Sissmann, O., Menguy, N., Saldi, G.D., Guyot, F., Martinez, I., Corvisier, J., Garcia, B., Machouk, I., Knauss, K.G., Hellmann, R., 2011. Influence of amorphous silica layer formation on the dissolution rate of olivine at 90°C and elevated pCO(2). Chem. Geol. 284, 193-209.

Davison, W., Seed, G., 1983. The kinetics of the oxidation of ferrous iron in synthetic and natural-waters. Geochim. Cosmochim. Acta 47, 67-79.

de Boer, W., Leveau, J.H.J., Kowalchuk, G.A., Gunnewiek, P., Abeln, E.C.A., Figge, M.J., Sjollema, K., Janse, J.D., van Veen, J.A., 2004. *Collimonas fungivorans* gen. nov., sp nov., a chitinolytic soil bacterium with the ability to grow on living fungal hyphae. Int. J. Syst. Evol. Microbiol. 54, 857-864.

Drever, J.I., Stillings, L.L., 1997. The role of organic acids in mineral weathering. Colloids. Surf. A Physicochem. Eng. Asp. 120, 167-181.

Duplay, J., Semhi, K., Errais, E., Imfeld, G., Babcsanyi, I., Perrone, T., 2014. Copper, zinc, lead and cadmium bioavailability and retention in vineyard soils (Rouffach, France): The impact of cultural practices. Geoderma 230, 318-328.

El Gh'Mari, A., 1995. Etude minéralogique, pétrophysique et géochimique de la dynamique d'altération d'un granite soumis au dépôts atmosphèriques acides (Bassin Versant du Strengbach, Vosges, France), PhD. Université Louis Pasteur.

Esther, J., Sukla, L.B., Pradhan, N., Panda, S., 2015. Fe (III) reduction strategies of dissimilatory iron reducing bacteria. Korean J. Chem. Eng. 32, 1-14.

Feger, K.-H., Brahmer, G., Zöttl, H.W., 1990. An integrated watershed/plot-scale study of element cycling in spruce ecosystems of the black forest. Water, Air, Soil Pollut. 54, 545-560.

Ferrier, K.L., Kirchner, J.W., Riebe, C.S., Finkel, R.C., 2010. Mineral-specific chemical weathering rates over millennial timescales: Measurements at Rio Icacos, Puerto Rico. Chem. Geol. 277, 101-114.

Fischer, C., Arvidson, R.S., Lüttge, A., 2012. How predictable are dissolution rates of crystalline material? Geochim. Cosmochim. Acta 98, 177-185.

Frey, B., Rieder, S.R., Brunner, I., Ploetze, M., Koetzsch, S., Lapanje, A., Brandl, H., Furrer, G., 2010. Weathering-associated bacteria from the Damma glacier forefield: physiological vapabilities and impact on granite dissolution. Appl. Environ. Microbiol. 76, 4788-4796.

Gaillardet, J., Dupre, B., Allegre, C.J., 1995. A global mass budget applied to the Congo basin rivers - Erosion rates and continental crust composition. Geochim. Cosmochim. Acta 59, 3469-3485.

Gaillardet, J., Dupré, B., Louvat, P., Allègre, C.J., 1999. Global silicate weathering and CO_2 consumption rates deduced from the chemistry of large rivers. Chem. Geol. 159, 3-30.

Ganor, J., Renznik, I.J., Rosenberg, Y.O., 2009. Organics in water-rock interactions, Thermodynamics and kinetics of water-rock interaction. Mineralogical Society of America, pp. 259-369.

Gerard, F., Clement, A., Fritz, B., Crovisier, J.L., 1996. Introduction of transport phenomena into the thermo-kinetic code KINDIS: The code KIRMAT. C. R. Acad. Sci., Serie II. Sciences de la Terre et des Planetes 322, 377-384.

Gin, S., Jegou, C., Frugier, P., Minet, Y., 2008. Theoretical consideration on the application of the Aagaard-Helgeson rate law to the dissolution of silicate minerals and glasses. Chem. Geol. 255, 14-24.

Gin, S., Jollivet, P., Fournier, M., Angeli, F., Frugier, P., Charpentier, T., 2015. Origin and consequences of silicate glass passivation by surface layers. Nat. Commun. 6, 6360.

Gleeson, D.B., Kennedy, N.M., Clipson, N., Melville, K., Gadd, G.M., McDermott, F.P., 2006. Characterization of bacterial community structure on a weathered pegmatitic granite. Microb. Ecol. 51, 526-534.

Goddéris, Y., Donnadieu, Y., 2009. Climatic plant power. Nature 460, 40.

Godderis, Y., Francois, L.M., Probst, A., Schott, J., Moncoulon, D., Labat, D., Viville, D., 2006. Modelling weathering processes at the catchment scale: The WITCH numerical model. Geochim. Cosmochim. Acta 70, 1128-1147.

Granier, A., Breda, N., Biron, P., Villette, S., 1999. A lumped water balance model to evaluate duration and intensity of drought constraints in forest stands. Ecol. Model. 116, 269-283.

Gruber, C., Zhu, C., Georg, R.B., Zakon, Y., Ganor, J., 2014. Resolving the gap between laboratory and field rates of feldspar weathering. Geochim. Cosmochim. Acta 147, 90-106.

Gutiérrez, J.L., Jones, C.G., 2006. Physical ecosystem engineers as agents of biogeochemical heterogeneity. BioScience 56, 227-236.

Harris, I., Jones, P.D., Osborn, T.J., Lister, D.H., 2014. Updated high-resolution grids of monthly climatic observations - the CRU TS3.10 Dataset. Int. J. Climatol. 34, 623-642.

Heckman, K., Welty-Bernard, A., Vazquez-Ortega, A., Schwartz, E., Chorover, J., Rasmussen, C., 2013. The influence of goethite and gibbsite on soluble nutrient dynamics and microbial community composition. Biogeochemistry 112, 179-195.

1139 Hedrich, S., Schlomann, M., Johnson, D.B., 2011. The iron-oxidizing proteobacteria.
1140 Microbiology-Sgm 157, 1551-1564.
1141 Hellmann, R., Tisserand, D., 2006. Dissolution kinetics as a function of the Gibbs free
1142 energy of reaction: An experimental study based on albite feldspar. Geochim. Cosmochim. Acta
1143 70, 364-383.
1144 Henri, P.A., Rommevaux-Jestin, C., Lesongeur, F., Mumford, A., Emerson, D.,
1145 Godfroy, A., Ménez, B., 2016. Structural iron (II) of basaltic glass as an energy source for
1146 zetaproteobacteria in an abyssal plain environment, off the mid Atlantic ridge. Front. Microbiol.
1147 6.
1148 Johnson, J., Aherne, J., Cummins, T., 2015. Base cation budgets under residue removal
1149 in temperate maritime plantation forests. For. Ecol. Manage. 343, 144-156.
1150 Johnstone, T.C., Nolan, E.M., 2015. Beyond iron: non-classical biological functions of
1151 bacterial siderophores. Dalton Trans. 44, 6320-6339.
1152 Jones, A.A., Bennett, P.C., 2014. Mineral microniches control the diversity of
1153 subsurface microbial populations. Geomicrobiol. J.31, 246-261.
1154 Jongmans, A.G., vanBreemen, N., Lundstrom, U., vanHees, P.A.W., Finlay, R.D.,
1155 Srinivasan, M., Unestam, T., Giesler, R., Melkerud, P.A., Olsson, M., 1997. Rock-eating fungi.
1156 Nature 389, 682-683.
1157 Kalinowski, B.E., Liermann, L.J., Brantley, S.L., Barnes, A., Pantano, C.G., 2000. X-
1158 ray photoelectron evidence for bacteria-enhanced dissolution of hornblende. Geochim.
1159 Cosmochim. Acta 64, 1331-1343.
1160 Kim, Y.H., Bae, B., Choung, Y.K., 2005. Optimization of biological phosphorus
1161 removal from contaminated sediments with phosphate-solubilizing microorganisms. J. Biosci.
1162 Bioeng. 99, 23-29.

1163 Klaminder, J., Lucas, R.W., Futter, M.N., Bishop, K.H., Kohler, S.J., Egnell, G.,
1164 Laudon, H., 2011. Silicate mineral weathering rate estimates: Are they precise enough to be
1165 useful when predicting the recovery of nutrient pools after harvesting? For. Ecol. Manage. 261,
1166 1-9.
1167 Knauss, K.G., Wolery, T.J., 1988. The dissolution kinetics of quartz as a function of pH
1168 and time at 70°C. Geochim. Cosmochim. Acta 52, 43-53.
1169 Lapanje, A., Wimmersberger, C., Furrer, G., Brunner, I., Frey, B., 2012. Pattern of
1170 elemental release during the granite dissolution can be changed by aerobic heterotrophic
1171 bacterial strains isolated from Damma glacier (central Alps) deglaciated granite sand. Microb.
1172 Ecol. 63, 865-882.
1173 Lasaga, A.C., 1998. Kinetic Theory in the Earth Sciences. Princeton University Press,
1174 New York.
1175 Lefèvre, Y., 1988. Les sols du bassin versant d'Aubure : caractérisation et facteurs de
1176 répartition. Ann. Sci. For. 45, 417-422.
1177 Lepleux, C., Turpault, M.P., Oger, P., Frey-Klett, P., Uroz, S., 2012. Correlation of the
1178 abundance of betaproteobacteria on mineral surfaces with mineral weathering in forest soils.
1179 Appl. Environ. Microbiol. 78, 7114-7119.
1180 Li, Z.B., Liu, L.W., Chen, J., Teng, H.H., 2016. Cellular dissolution at hypha- and spore-
1181 mineral interfaces revealing unrecognized mechanisms and scales of fungal weathering.
1182 Geology 44, 319-322.
1183 Lower, S.K., Hochella, M.F., Beveridge, T.J., 2001. Bacterial recognition of mineral
1184 surfaces: nanoscale interactions between *Shewanella* and α-FeOOH. Science 292, 1360-1363.
1185 Lucas, R.W., Klaminder, J., Futter, M.N., Bishop, K.H., Egnell, G., Laudon, H.,
1186 Hogberg, P., 2011. A meta-analysis of the effects of nitrogen additions on base cations:
1187 Implications for plants, soils, and streams. For. Ecol. Manage. 262, 95-104.

1188 Lüttge, A., Arvidson, R.S., Fischer, C., 2013. A Stochastic Treatment of Crystal
1189 Dissolution Kinetics. Elements 9, 183-188.
1190 Maher, K., DePaolo, D.J., Lin, J.C.-F., 2004. Rates of silicate dissolution in deep-sea
1191 sediment: In situ measurement using 234U/238U of pore fluids. Geochim. Cosmochim. Acta
1192 68, 4629-4648.
1193 Maher, K., Steefel, C.I., White, A.F., Stonestrom, D.A., 2009. The role of reaction
1194 affinity and secondary minerals in regulating chemical weathering rates at the Santa Cruz Soil
1195 Chronosequence, California. Geochim. Cosmochim. Acta 73, 2804-2831.
1196 Mailloux, B.J., Alexandrova, E., Keimowitz, A.R., Wovkulich, K., Freyer, G.A.,
1197 Herron, M., Stolz, J.F., Kenna, T.C., Pichler, T., Polizzotto, M.L., Dong, H., Bishop, M.,
1198 Knappett, P.S.K., 2009. Microbial mineral weathering for nutrient acquisition releases arsenic.
1199 Appl. Environ. Microbiol. 75, 2558-2565.
1200 Mitchell, A.C., Lafreniere, M.J., Skidmore, M.L., Boyd, E.S., 2013. Influence of
1201 bedrock mineral composition on microbial diversity in a subglacial environment. Geology 41,
1202 855-858.
1203 Negrel, P., Allegre, C.J., Dupre, B., Lewin, E., 1993. Erosion sources determined by
1204 inversion of major and trace element ratios and strontium isotopic ratios in river water - The
1205 congo basin case. Earth Planet. Sci. Lett.120, 59-76.
1206 Newman, D.K., Kolter, R., 2000. A role for excreted quinones in extracellular electron
1207 transfer. Nature 405, 94-97.
1208 Nugent, M.A., Brantley, S.L., Pantano, C.G., Maurice, P.A., 1998. The influence of
1209 natural mineral coatings on feldspar weathering. Nature 395, 588-591.
1210 Odum, E.P., 1950. Bird populations of the Highlands (North Carolina) plateau in
1211 relation to plant succession and avian invasion. Ecology 31, 587-605.

Oksanen J., F. Blanchet G., Kindt R., Legendre P., Minchin P. R., O'Hara R. B., Simpson G. L., Solymos P., Stevens M. H. H. and Wagner H. (2013) Vegan: Community Ecology Package. R package version 2.0-8, http://CRAN.R-project.org/package=vegan.

Or, D., Phutane, S., Dechesne, A., 2007. Extracellular polymeric substances affecting pore-scale hydrologic conditions for bacterial activity in unsaturated soils. Vadose Zone J. 6, 298-305.

Paces, T., 1983. Rate constants of dissolution derived from the measurements of mass balance in hydrological catchments. Geochim. Cosmochim. Acta 47, 1855-1863.

Palandri, J.L., Kharaka, Y.K., 2004. A compilation of rate parameters of water-mineral interaction kinetics for application to geochemical modeling, in: Survey, U.S.G. (Ed.), U.S. Geological Survey, Open File Report. U.S. Geological Survey, Open File Report, p. 70.

Pierret, M.C., Stille, P., Prunier, J., Viville, D., Chabaux, F., 2014. Chemical and U–Sr isotopic variations in stream and source waters of the Strengbach watershed (Vosges mountains, France). Hydrol. Earth Syst. Sci. 18, 3969-3985.

Reguera, G., McCarthy, K.D., Mehta, T., Nicoll, J.S., Tuominen, M.T., Lovley, D.R., 2005. Extracellular electron transfer via microbial nanowires. Nature 435, 1098-1101.

Rimstidt, J.D., Brantley, S.L., Olsen, A.A., 2012. Systematic review of forsterite dissolution rate data. Geochim. Cosmochim. Acta 99, 159-178.

Roden, E.E., Kappler, A., Bauer, I., Jiang, J., Paul, A., Stoesser, R., Konishi, H., Xu, H.F., 2010. Extracellular electron transfer through microbial reduction of solid-phase humic substances. Nat. Geosci. 3, 417-421.

Roelandt, C., Godderis, Y., Bonnet, M.P., Sondag, F., 2010. Coupled modeling of biospheric and chemical weathering processes at the continental scale. Global Biogeochemical Cycles 24.

Saha, R., Saha, N., Donofrio, R.S., Bestervelt, L.L., 2013. Microbial siderophores: a mini review. J. Basic Microbiol. 53, 303-317.

Singh, R., Beriault, R., Middaugh, J., Hamel, R., Chenier, D., Appanna, V.D., Kalyuzhnyi, S., 2005. Aluminum-tolerant Pseudomonas fluorescens: ROS toxicity and enhanced NADPH production. Extremophiles 9, 367-373.

Sitch, S., Smith, B., Prentice, I.C., Arneth, A., Bondeau, A., Cramer, W., Kaplan, J.O., Levis, S., Lucht, W., Sykes, M.T., Thonicke, K., Venevsky, S., 2003. Evaluation of ecosystem dynamics, plant geography and terrestrial carbon cycling in the LPJ dynamic global vegetation model. Glob. Chang. Biol. 9, 161-185.

Solden, L., Lloyd, K., Wrighton, K., 2016. The bright side of microbial dark matter: lessons learned from the uncultivated majority. Curr. Opin. Microbiol.31, 217-226.

Steefel, C., Lasaga, A.C., 1994. A coupled model for transport of multiple chemical species and kinetic precipitation/dissolution reactions with application to reactive flow in single phase hydrothermal systems Am. J. Sci. 294, 529-592.

Sverdrup, H., 1990. The kinetics of Chemical Weathering. Lund University Press, Lund, Sweden.

Sverdrup, H., Warfvinge, P., 1993. Calculating field weathering rates using a mechanistic geochemical model PROFILE. Appl. Geochem.8, 273-283.

Sverdrup, H., Warfvinge, P., 1995. Estimating field weathering rates using laboratory kinetics, Chemical Weathering Rates of Silicate Minerals, pp. 485-541.

Taylor, A.S., Blum, J.D., Lasaga, A.C., 2000. The dependence of labradorite dissolution and Sr isotope release rates on solution saturation state. Geochim. Cosmochim. Acta 64, 2389-2400.

Tester, J.W., Worley, W.G., Robinson, B.A., Grigsby, C.O., Feerer, J.L., 1994. Correlating quartz dissolution kinetics in pure water from 25 to 625°C. Geochim. Cosmochim. Acta 58, 2407-2420.

Ullman, W.J., Kirchman, D.L., Welch, S.A., Vandevivere, P., 1996. Laboratory evidence for microbially mediated silicate mineral dissolution in nature. Chem. Geol. 132, 11-17.

Uroz, S., Calvaruso, C., Turpault, M.-P., Frey-Klett, P., 2009. Mineral weathering by bacteria: ecology, actors and mechanisms. Trends Microbiol. 17, 378-387.

Uroz, S., Calvaruso, C., Turpault, M.P., Pierrat, J.C., Mustin, C., Frey-Klett, P., 2007. Effect of the mycorrhizosphere on the genotypic and metabolic diversity of the bacterial communities involved in mineral weathering in a forest soil. Appl. Environ. Microbiol. 73, 3019-3027.

Uroz, S., Kelly, L.C., Turpault, M.P., Lepleux, C., Frey-Klett, P., 2015. The Mineralosphere concept: mineralogical control of the distribution and function of mineral-associated bacterial communities. Trends Microbiol. 23, 751-762.

Uroz, S., Turpault, M.P., Delaruelle, C., Mareschal, L., Pierrat, J.C., Frey-Klett, P., 2012. Minerals affect the specific diversity of forest soil bacterial communities. Geomicrobiol. J.29, 88-98.

van der Heijden, G., Legout, A., Pollier, B., Mareschal, L., Turpault, M.P., Ranger, J., Dambrine, E., 2013. Assessing Mg and Ca depletion from broadleaf forest soils and potential causes - A case study in the Morvan Mountains. For. Ecol. Manage. 293, 65-78.

van Scholl, L., Kuyper, T.W., Smits, M.M., Landeweert, R., Hoffland, E., van Breemen, N., 2008. Rock-eating mycorrhizas: their role in plant nutrition and biogeochemical cycles. Plant Soil 303, 35-47.

Vassilev, N., Vassileva, M., Nikolaeva, I., 2006. Simultaneous P-solubilizing and biocontrol activity of microorganisms: potentials and future trends. Appl. Microbiol. Biotechnol. 71, 137-144.

Violette, A., Goddéris, Y., Maréchal, J.-C., Riotte, J., Oliva, P., Kumar, M.S.M., Sekhar, M., Braun, J.-J., 2010. Modelling the chemical weathering fluxes at the watershed scale in the Tropics (Mule Hole, South India): Relative contribution of the smectite/kaolinite assemblage versus primary minerals. Chem. Geol. 277, 42-60.

Viville, D., Chabaux, F., Stille, P., Pierret, M.C., Gangloff, S., 2012. Erosion and weathering fluxes in granitic basins: The example of the Strengbach catchment (Vosges massif, eastern France). Catena 92, 122-129.

Walters, W.A., Caporaso, J.G., Lauber, C.L., Berg-Lyons, D., Fierer, N., Knight, R., 2011. PrimerProspector: de novo design and taxonomic analysis of barcoded polymerase chain reaction primers. Bioinformatics 27, 1159-1161.

Ward, J.H., 1963. Hierarchical Grouping to Optimize an Objective Function. J. Am. Stat. Assoc. 58, 236-244.

Warfvinge, P., Sverdrup, H., 1988. Soil liming as a measure to mitigate acid runoff. Water Resour. Res.24, 701-712.

Warfvinge, P., Sverdrup, H., 1992. Calculating critical loads of acid deposition with PROFILE - a steady-state soil chemistry model. Water, Air, Soil Pollut. 63, 119-143.

Weber, K.A., Achenbach, L.A., Coates, J.D., 2006. Microorganisms pumping iron: anaerobic microbial iron oxidation and reduction. Nat. Rev. Microbiol. 4, 752-764.

Welch, S.A., Barker, W.W., Banfield, J.F., 1999. Microbial extracellular polysaccharides and plagioclase dissolution. Geochim. Cosmochim. Acta 63, 1405-1419.

Welch, S.A., Ullman, W.J., 1993. The effect of organic acids on plagioclase dissolution raes and stoichiometry. Geochim. Cosmochim. Acta 57, 2725-2736.

White, A.F., Brantley, S.L., 2003. The effect of time on the weathering of silicate minerals: why do weathering rates differ in the laboratory and field? Chem. Geol. 202, 479-506.

Wild, B., Daval, D., Guyot, F., Knauss, K.G., Pollet-Villard, M., Imfeld, G., 2016. pH-dependent control of feldspar dissolution rate by altered surface layers. Chem. Geol. 442, 148-159.

Wild, B., Imfeld, G., Guyot, F., Daval, D., 2018. Early stages of bacterial community adaptation to silicate aging. Geology 46, 555-558.

Wu, L., Jacobson, A.D., Chen, H.-C., Hausner, M., 2007. Characterization of elemental release during microbe-basalt interactions at T=28 degrees C. Geochim. Cosmochim. Acta 71, 2224-2239.

Wu, L., Jacobson, A.D., Hausner, M., 2008. Characterization of elemental release during microbe-granite interactions at T=28 °C. Geochim. Cosmochim. Acta 72, 1076-1095.

Yarza, P., Yilmaz, P., Pruesse, E., Glockner, F.O., Ludwig, W., Schleifer, K.-H., Whitman, W.B., Euzeby, J., Amann, R., Rossello-Mora, R., 2014. Uniting the classification of cultured and uncultured bacteria and archaea using 16S rRNA gene sequences. Nat. Rev. Microbiol. 12, 635-645.

Yeh, G.T., Tripathi, V.S., 1991. A Model for Simulating Transport of Reactive Multispecies Components: Model Development and Demonstration. Water Resour. Res.27, 3075-3094.

Yu, C., Lavergren, U., Peltola, P., Drake, H., Bergbäck, B., Åström, M.E., 2014. Retention and transport of arsenic, uranium and nickel in a black shale setting revealed by a long-term humidity cell test and sequential chemical extractions. Chem. Geol. 363, 134-144.

Zhu, C., Liu, Z., Schaefer, A., Wang, C., Zhang, G., Gruber, C., Ganor, J., Georg, R.B., 2014. Silicon Isotopes as a New Method of Measuring Silicate Mineral Reaction Rates at Ambient Temperature. Procedia Earth and Planet. Sci. 10, 189-193.

8. FIGURE CAPTIONS

Fig. 1: Compartments of the critical zone probed at the Strengbach catchment (A). Soil profile of the beech plot (B) and corresponding reactivity probes after 20 months of incubation into the A horizon (C) and the C horizon (D). Overview of the setup used to expose samples to atmospheric weathering (E) onto a Polytetrafluoroethylene (PTFE) plate (F). Reactivity probe after 20 months of incubation at the weather station (G). Experimental setup used to immerse samples into the Strengbach stream at the outlet (H) with flow-through PTFE holders (I). Reactivity probe after 20 months of incubation into the Strengbach stream (J). White and black crosses indicate the locations of the samples.

Fig. 2: Exchangeable Mg (A) and Ca (B) as determined by ammonium acetate extractions on samples of the soil profile of the beech plot collected on 11/18/2013 and 12/02/2014 (see Table A.3). For comparison, green and orange plots represent corresponding concentrations measured at the experimental plot of Breuil-Chenue (Morvan, France) before and 30 years after deforestation respectively (van der Heijden *et al.*, 2013).

Fig. 3: Labradorite sample collected after 9 months of incubation in the C horizon of the soil profile of the beech plot at the Strengbach catchment. Stereo microscope image acquired before removal of the Room Temperature Vulcanizing (RTV) glue mask (A), vertical scanning

interferometry (VSI) surface topography after cleaning (B) and interpretation in terms of surface retreat overimposed on stitched VSI images before removal of the RTV glue mask (visible inside the circled area) of the same portion of the sample (C). Black arrowheads in (B) indicate zones where the global retreat of the surface at the previous location of the mask is visible. White arrows indicate another boundary of the mask indicated by a residue of RTV glue. Striped zone in (C) correspond to a location where natural fluid circulation likely occurred (see text).

Fig. 4: Olivine samples after 9 months of incubation in the A horizon of the soil profile of the beech plot at the Strengbach catchment. Stereo microscope image acquired before removal of the RTV glue mask (A) and stitched VSI images of the surface after cleaning (B). Dashed lines indicate the boundary of zones interpreted in (C) as portions of the olivine surface that were either masked (1), including traces of possible fluid circulation (2), or the rest of the mineral surface exposed to the soil environment (3). Red box in C indicates the portion of the surface imaged by stereo microscope right after incubation (D) or by VSI before (E) and after (F) 9 months of incubation. Striped zone in (D), (E) and (F) correspond to the masked area. Profiles at the boundary between zones 2 and 3 and zones 1 and 2 (indicated by a red arrowhead) before (in blue) and after (in red) 9 months of incubation are reported in (G) and (H) respectively..

Fig. 5: Detail of the surface topography of an olivine reactivity probe before (A) and after (B) 9 months of incubation in the A horizon of the soil profile at the beech plot. Superposition of profiles before (black) and after (red) incubation (C) and corresponding surface retreat (D). This analysis reveals a global retreat of the surface (red arrow, C; dashed area, D) and local alteration features (green arrow, C; dotted area, D).

Fig. 6: Detail of the surface topography of an olivine reactivity probe after 9 months of incubation in the A horizon of the soil profile of the

plot (A, C). Its interpretation in terms of weathering fluxes, as estimated from topography and rate spectra (D, E) following the approach developed in (Fischer et al., 2012), is displayed (B). It reveals zones impacted by the global retreat of the surface (green) with respect to the initial masked surface area (black, M) and local alteration features (red). The contribution of zones related to the initial topography is highlighted in grey.

Fig. 7: Temporal variations of pH (A), temperature (B), and dissolution rates (C) of olivine and labradorite modeled by WITCH for two soil horizons at the beech plot of the Strengbach catchment. The greyed areas correspond to the incubation period of the probes.

Fig. 8: Relative proportions of bacterial phyla analyzed in the environmental probes incubated in several compartments of the critical zone at the Strengbach catchment. Mean values over all samples incubated at a given location. “Others” category gathers the 20 less represented phyla together with sequences which could not be classified with a sufficient degree of confidence.

Fig. 9: Statistical analyses of the composition of microbial communities of the environmental probes incubated at the weather station (A,B), in the A horizon (C,D), in the C horizon (E,F), and in the stream (G,H). Analyzed samples include the mineralosphere of labradorite (L), olivine (O) and quartz (Q), as well as microbial communities from environmental matrices (E, either soil or stream sediments) and empty test bags (B). Trees correspond to the aggregation of OTUs at the species level with the Ward method on the basis of Bray-Curtis distances (A, C, E, G). Principal coordinate analyses (PCoA) of the relative abundance of the 16S rRNA genes with colors corresponding to the clusters determined with the Ward method. Crosses match to

a posteriori projection of OTUs corresponding to *Collimonas* sp. (1), *Burkholderia* sp. (2), *Pseudomonas* sp. (3), *Janthinobacterium* sp. (4), *Leifsonia* sp. (5), *Polaromonas* sp. (6), *Sphingomonas* sp. (7), *Arthrobacter* sp. (8).

Fig. 10: Detail of the surface topography of an olivine reactivity probe before (A) and after (B) 20 months of incubation at the weather station. Superposition of profiles before (black) and after (red) incubation (C) and corresponding surface retreat (D). 3D plot of the surface after incubation (B) with masked (M) zones (E).

Fig. 11: Evolutions of the $f(\Delta G_r)$ term, which describes the effect of the distance from equilibrium of the solution on mineral dissolution rate, and of the surface retreats for olivine and labradorite predicted by the WITCH model for the A and C horizons of the soil profile (A). The period highlighted in grey corresponds to the incubation of the samples. The $f(\Delta G_r)$ function is equal to ~1 for all conditions except for labradorite in the C horizon when the $rate - \Delta G_r$ relation is described by the model of Taylor *et al.* (2000). Squares and diamonds in panels (B)-(D) represent *measured* surface retreats for samples incubated in the A and C horizons, respectively. Continuous curves represent *predicted* surface retreats based on outputs from the WITCH model. Corrected curves take into account fluid-mineral contact time and are based on ($f_2(\Delta G_r)$ function (see text). This figure stresses the amplitude of the field-laboratory discrepancy. The error bars are smaller than the size of symbols.

Fig. 12: Relative proportions of *Pseudomonas* sp., *Burkholderia* sp., *Collimonas* sp. (A), and *Arthrobacter* sp., *Leifsonia* sp., *Janthinobacterium* sp., et *Polaromonas* sp. (B), in the mineralospheres of quartz (Q), labradorite (L) and olivine (O), as well as in environmental samples (E) or empty bags (B). This figure illustrates that the proportion of genera known for

1431 their mineral weathering ability in pedological context is increased in the microbial
1432 communities of the environmental probes compared to those recovered from their respective
1433 surrounding environmental matrix.
1434
1435 **9. TABLE CAPTIONS**
1436
1437 Table 1: Global retreat of the surface of labradorite Δ_z and associated dissolution rate r
1438 measured *in-situ* in the field (F) or issued from WITCH simulations from kinetic rate laws
1439 determined in the laboratory (L), based on the transition state theory. Values between
1440 parentheses are based on a rate - ΔG_r relationship by Taylor *et al.* (2000). Predicted extent of
1441 reaction ξ and associated field-laboratory discrepancies $\Delta_{L/F}$. n.d. could not be estimated based
1442 on the methodology proposed here, since expected retreats were lower than measurable retreats
1443 due to the quality of the polishing of the corresponding samples.
1444
1445 Table 2: Global retreat of the surface of olivine Δ_z and associated dissolution rate r measured
1446 *in-situ* in the field (F) or issued from WITCH simulations from kinetic rate laws determined in
1447 the laboratory (L), based on the transition state theory. Predicted extent of reaction ξ and
1448 associated field-laboratory discrepancies $\Delta_{L/F}$. * retreat determined on a zone with no specific
1449 feature proving fluid circulation. ** possibly of biotic origin (see text).

Table 1

Sample	Context	incubation duration	Δ_Z^F	r_F	T	pH	Δ_Z^L	r_L	ξ	$\Delta_{L/F}$
				Labradorite						
		[months]	*[nm]*	*[mol.m^{-2}.s^{-1}]*	*[°C]*		*[nm]*	*[mol.m^{-2}.s^{-1}]*	*[mol.m^{-2}]*	
ML9	Weather Station	9	2*	8.59E-13	7.1	5.4	4.4	1.88E-12	4.49E-05	2.2
ML20	Weather Station	20	2*	3.84E-13	7.1	5.4	9.8	1.88E-12	1.01E-04	4.9
AL9a	A horizon	9	2*	8.59E-13	6.1	4.2	30.6	1.31E-11	2.93E-04	15.3
AL9b	A horizon	9	4.5	1.99E-12	6.1	4.2	30.3	1.34E-11	2.87E-04	6.7
AL20	A horizon	20	1.1*	2.11E-13	6.1	4.2	59.4	1.14E-11	5.68E-04	54.0
CL9a	C horizon	9	1.5*	6.44E-13	6.1	5.2	6.2 (1.7)	2.68E-12 (7.24E-13)	3.26E-05	4.1 (1.1)
CL9b	C horizon	9	1*	4.42E-13	6.1	5.2	6.1 (1.6)	2.72E-12 (7.24E-13)	3.16E-05	6.1 (1.6)
CL9c	C horizon	9	2.5*	1.11E-12	6.1	5.2	6.1 (1.6)	2.72E-12 (7.24E-13)	3.16E-05	2.4 (0.7)
CL20	C horizon	20	1.5*	2.88E-13	6.1	5.2	11.2 (3.1)	2.17E-12 (5.85E-13)	5.95E-05	7.5 (2.0)
EL9a	Stream	9	5*	2.15E-12	5.8	6.5	0.8	3.55E-13	8.45E-06	n.d.
EL9b	Stream	9	4*	1.77E-12	5.8	6.5	0.8	3.55E-13	8.21E-06	n.d.
EL20	Stream	20	1*	1.92E-13	5.8	6.5	1.8	3.55E-13	1.89E-05	1.8

Table 2

Sample	Context	incubation duration [months]	Olivine Δ_z^F [nm]	r_F [mol.m^{-2}.s^{-1}]	T [°C]	pH	Δ_z^L [nm]	r_L [mol.m^{-2}.s^{-1}]	ξ [mol.m^{-2}]	$\Delta_{L/F}$
MO9	Weather Station	9	1*	9.38E-13	7.1	5.4	83.8	7.87E-11	1.70E-03	84
MO20	Weather Station	20	171	7.17E-11	7.1	5.4	187.7	7.87E-11	3.82E-03	1
AO9	A horizon	9	24.19	2.27E-11	6.1	4.2	407.2	3.82E-10	8.53E-03	17
AO20	A horizon	20	3**	1.26E-12	6.1	4.2	809.6	3.39E-10	1.71E-02	270
CO9	C horizon	9	1.5	1.41E-12	6.1	5.2	112.1	1.05E-10	1.48E-03	75
CO20	C horizon	20	2*	8.38E-13	6.1	5.2	211.1	8.85E-11	2.75E-03	106
EO9	Stream	9	2.5	2.35E-12	5.8	6.5	21.7	2.04E-11	4.53E-04	9
EO20	Stream	20	2.5*	1.05E-12	5.8	6.5	48.6	2.04E-11	1.01E-03	19

Figure 1

Click here to download high resolution image

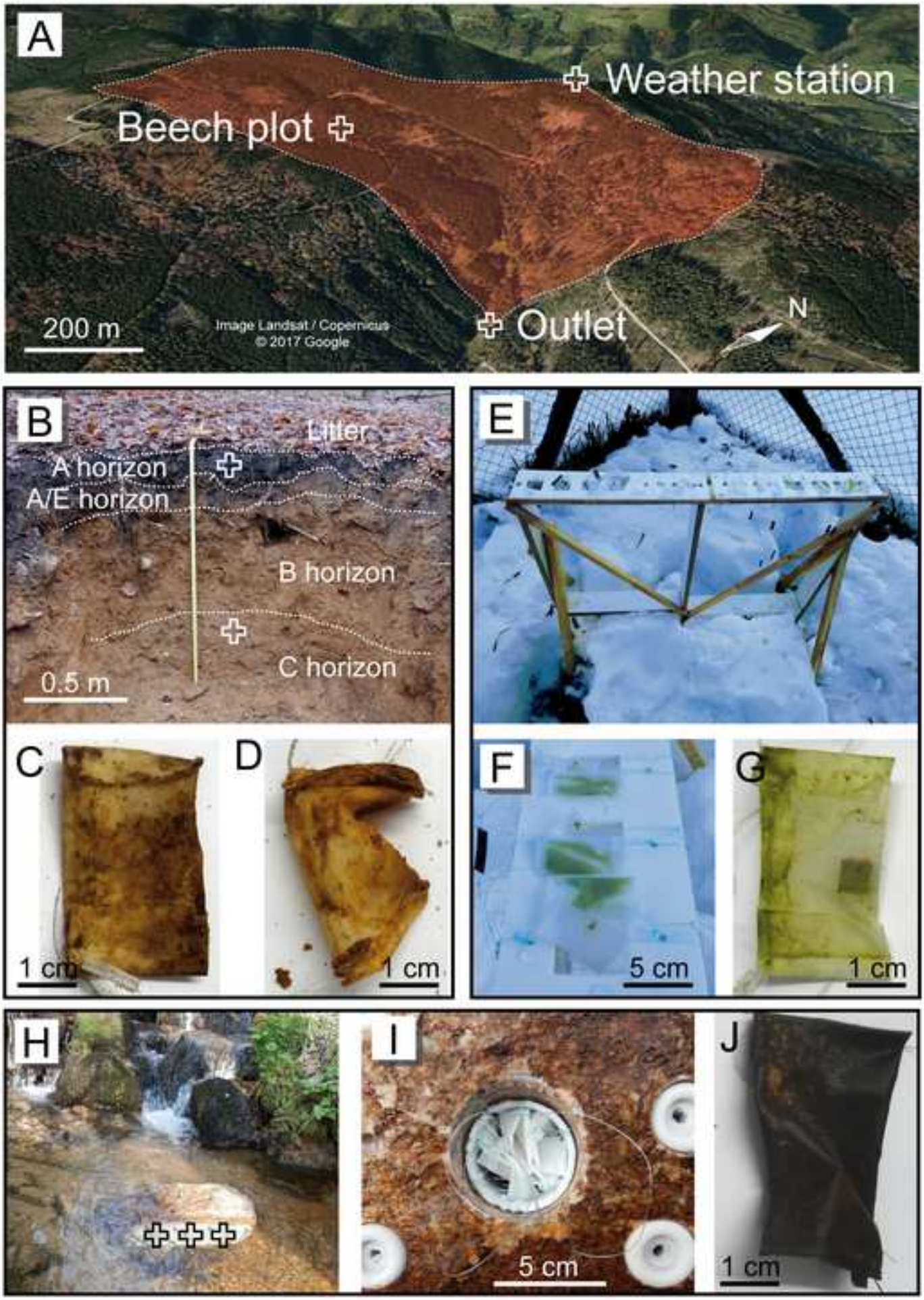

Figure 2

Click here to download high resolution image

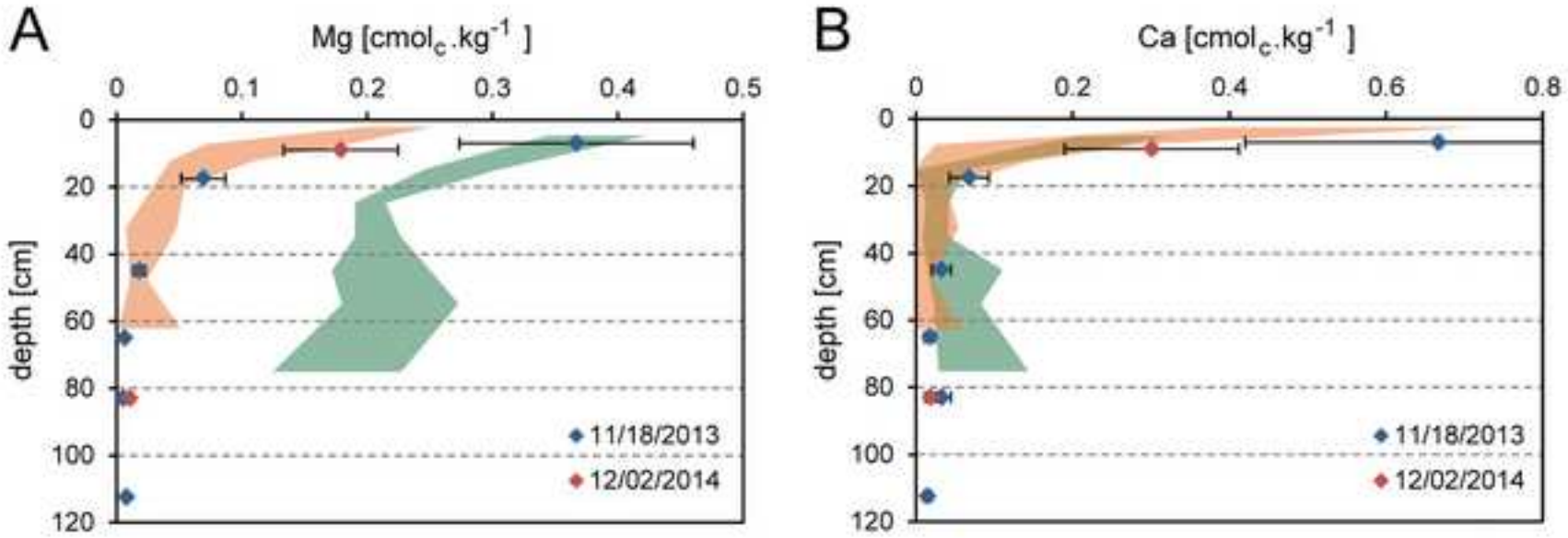

Figure 3

Click here to download high resolution image

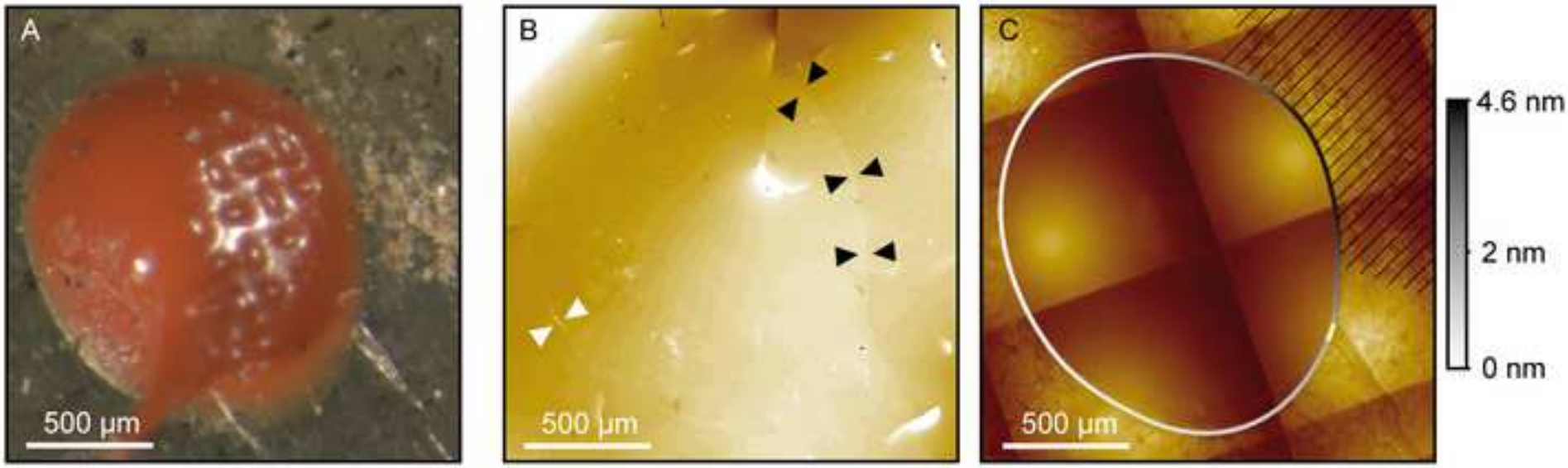

Figure 4

Click here to download high resolution image

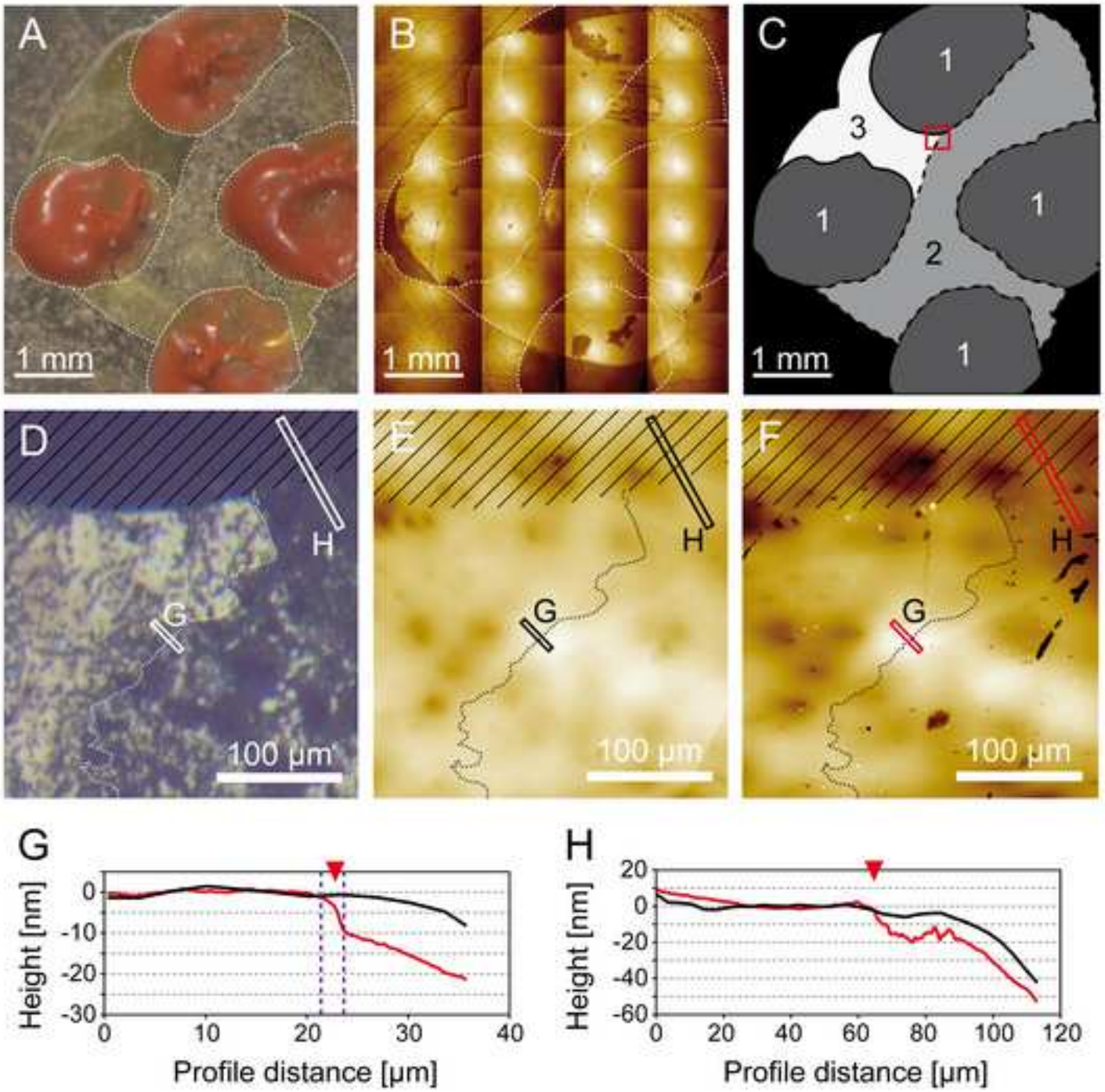

Figure 5

Click here to download high resolution image

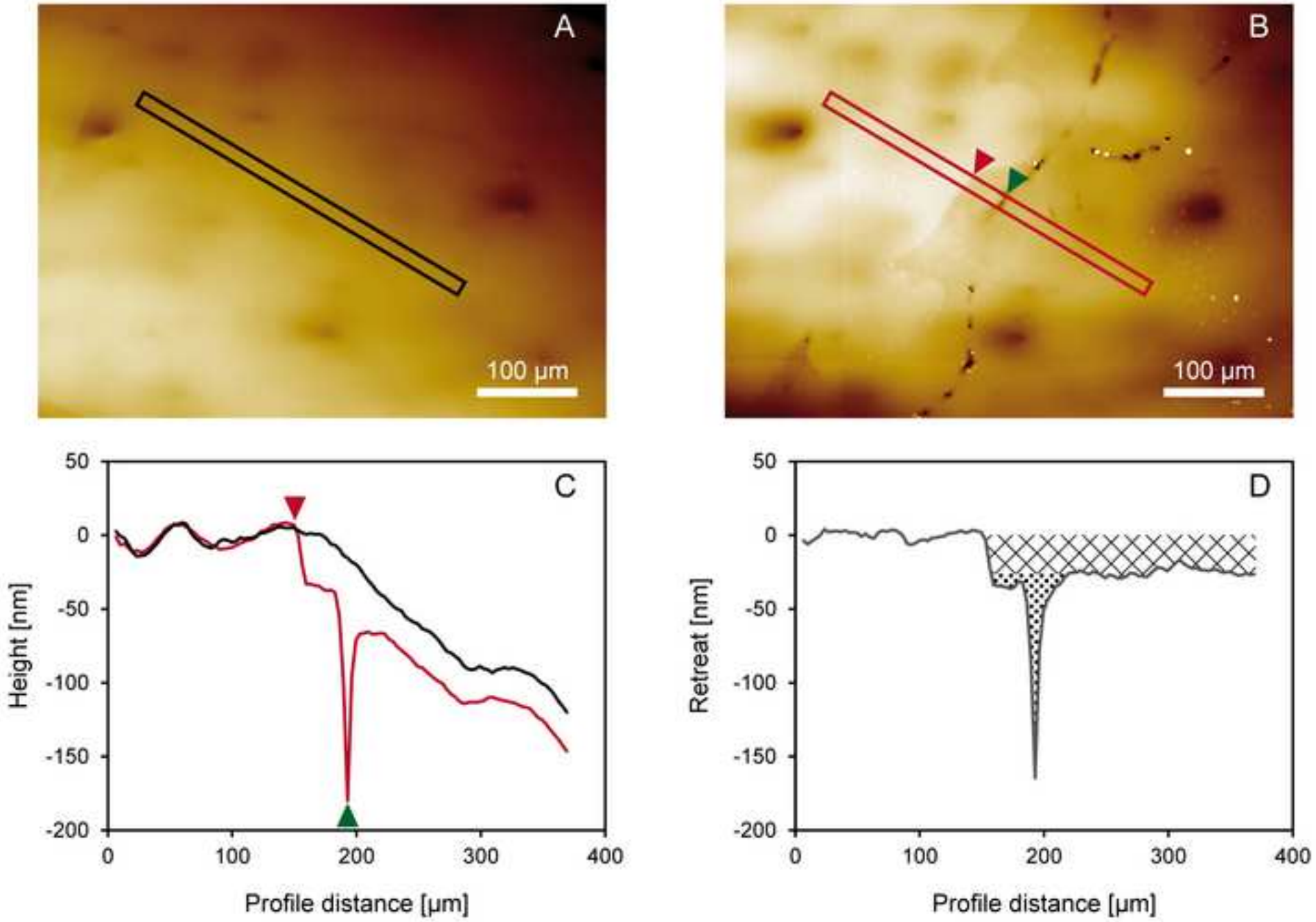

Figure 6

Click here to download high resolution image

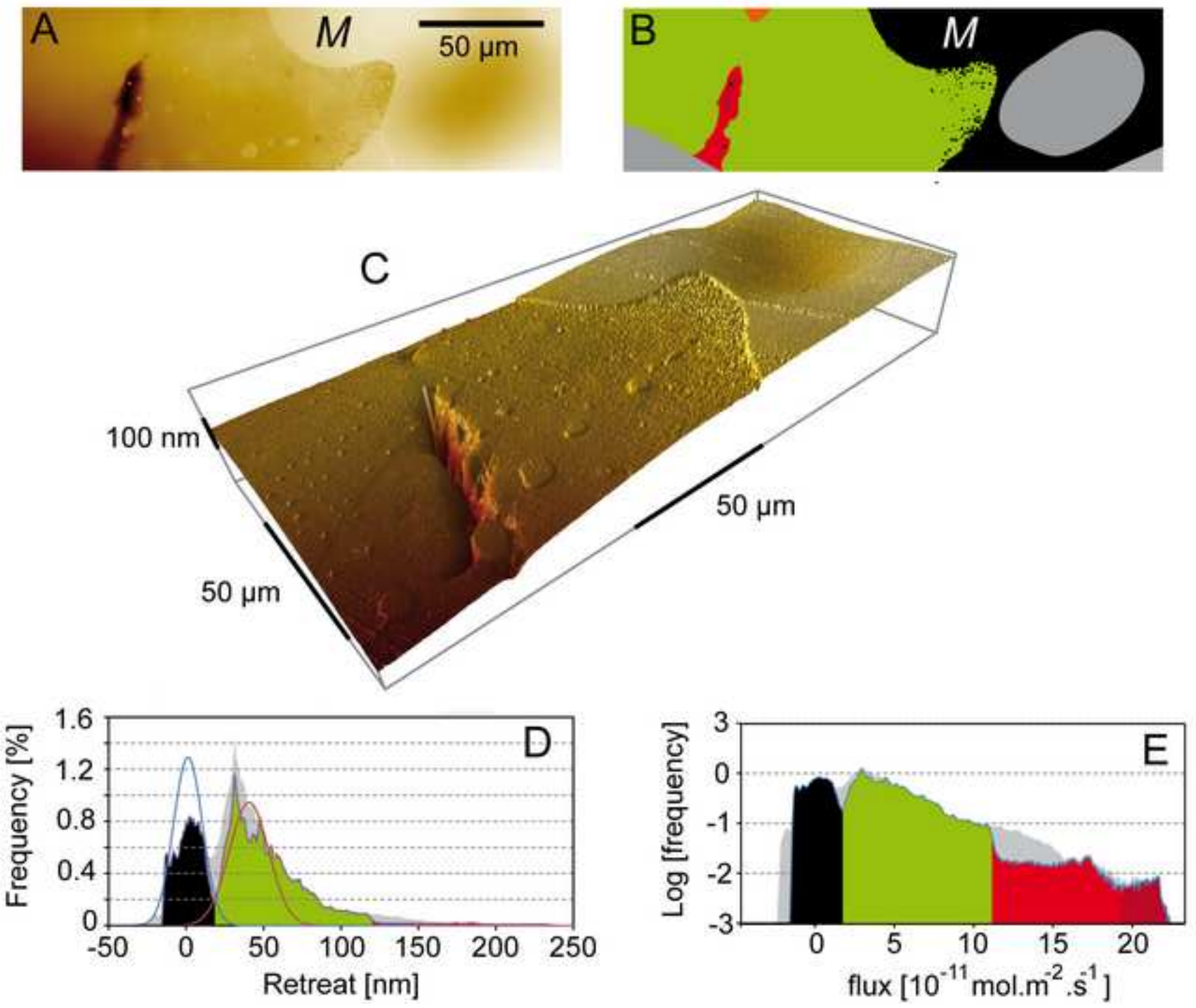

Figure 7

Click here to download high resolution image

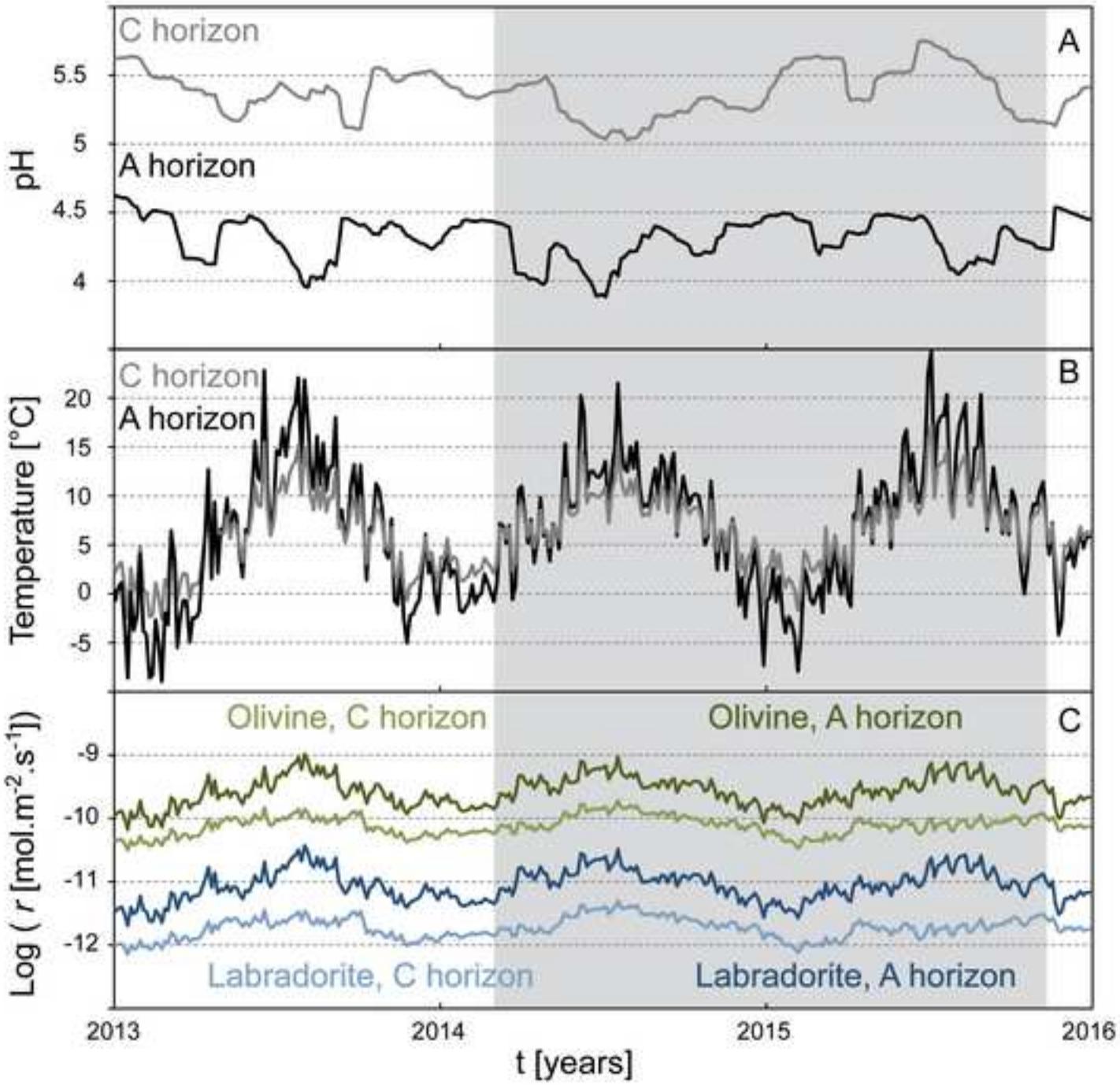

Figure 8

Click here to download high resolution image

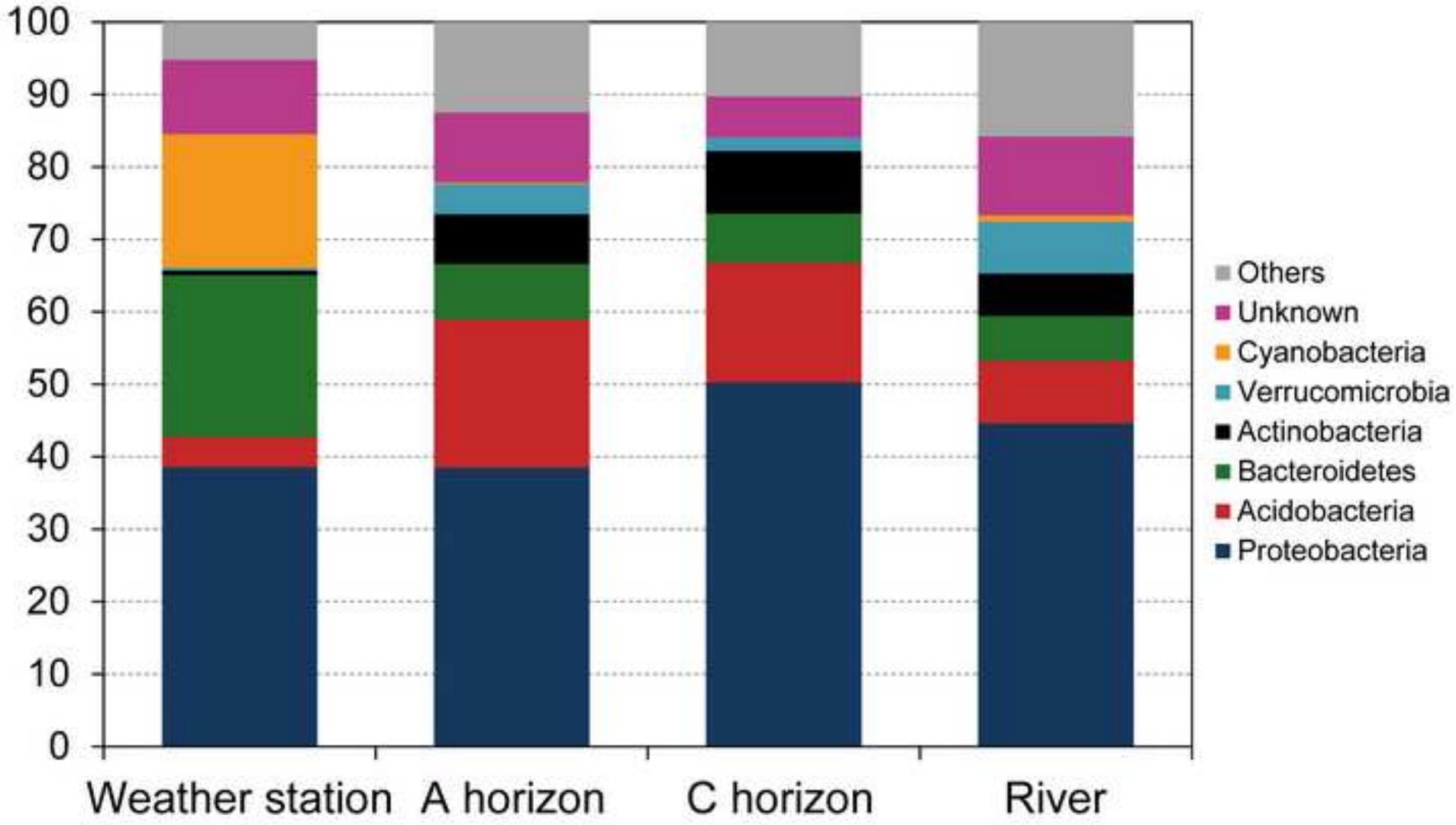

Figure 9

Click here to download high resolution image

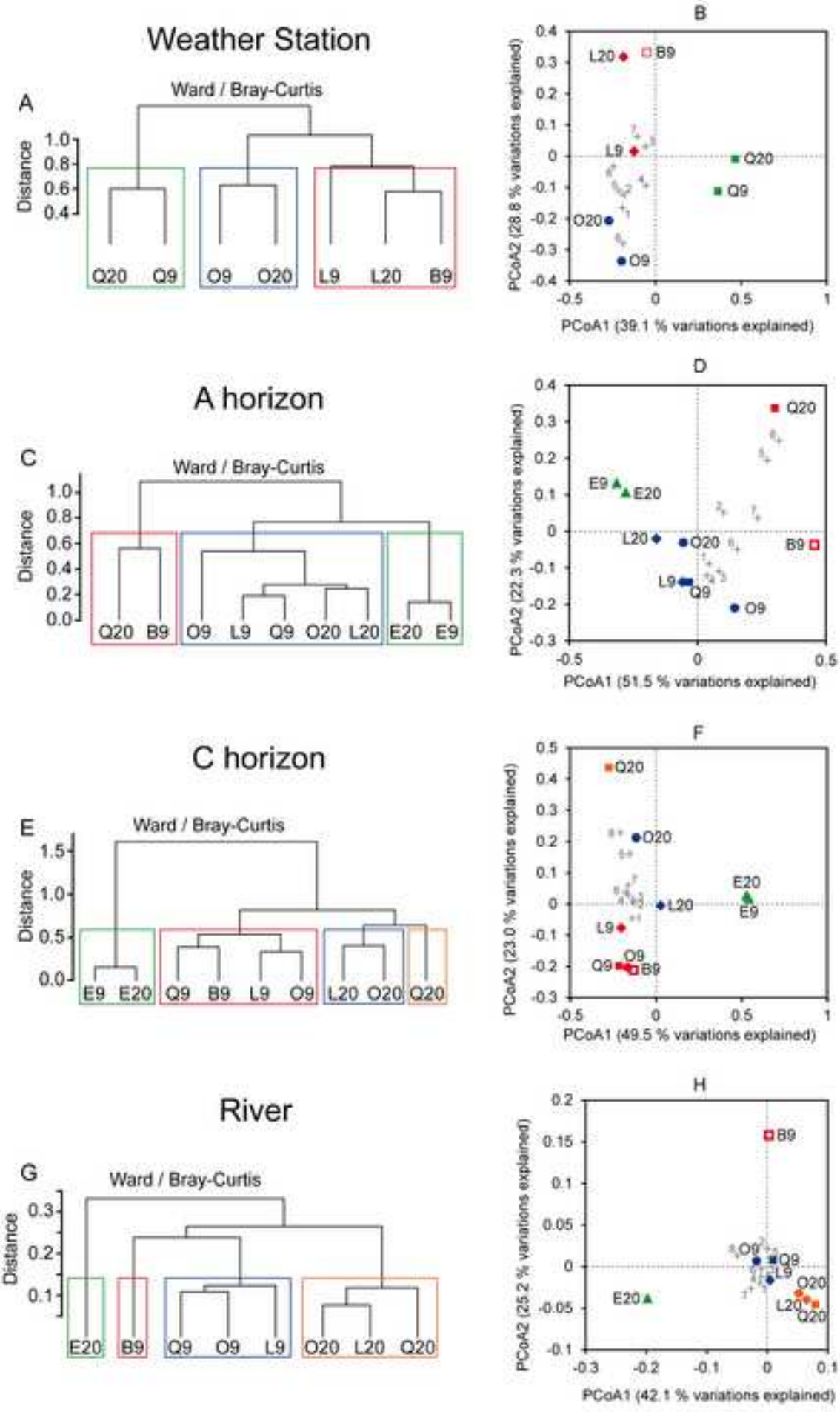

Figure 10

Click here to download high resolution image

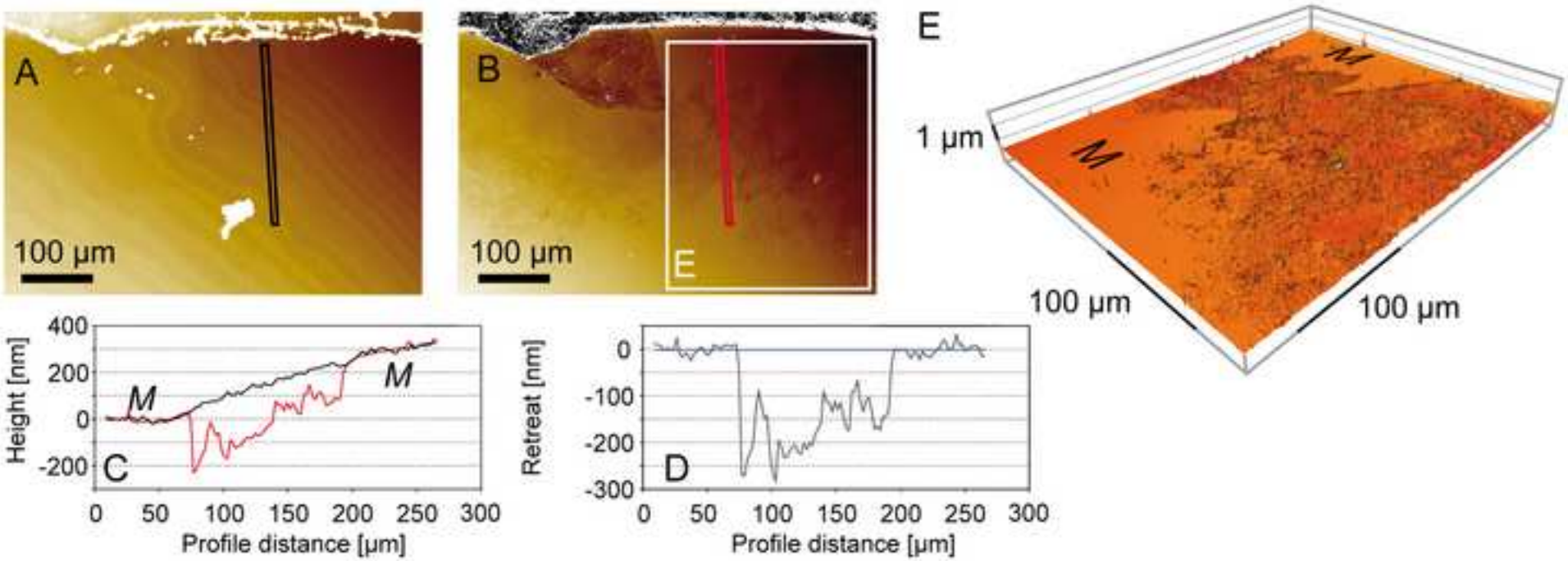

Figure 11
Click here to download high resolution image

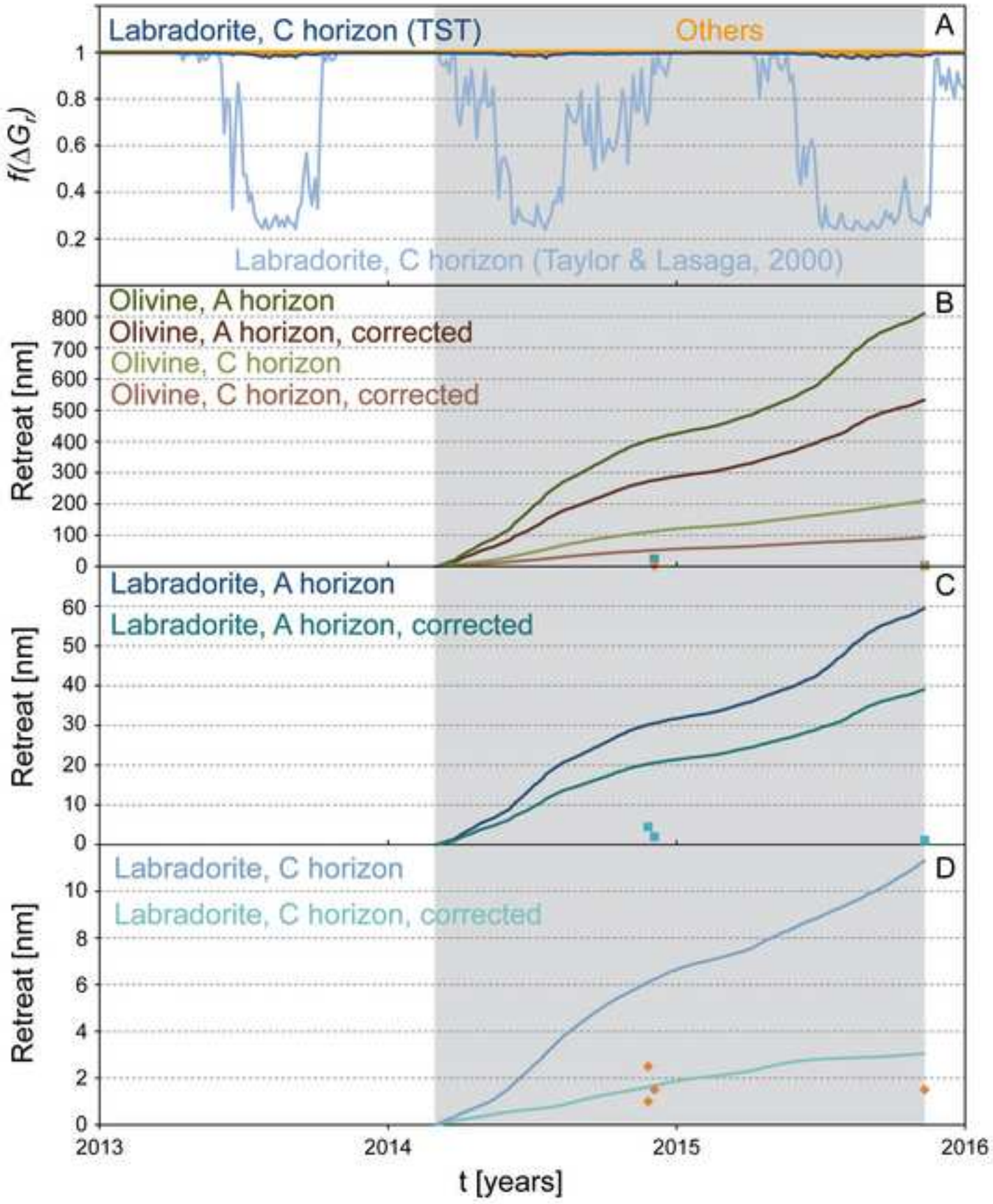

Figure 12

Click here to download high resolution image